

Visual binary stars with known orbits in Gaia EDR3

Dmitry Chulkov,¹* Oleg Malkov¹

¹INASAN, 48 Pyatnitskaya St., Moscow 119017, Russia

Accepted XXX. Received YYY; in original form ZZZ

ABSTRACT

3350 objects from the Sixth catalog of orbits of visual binary stars (ORB6) are investigated to validate *Gaia* EDR3 parallaxes and provide mass estimates for the systems. We show that 2/3 of binaries with 0.2 – 0.5 arcsec separation are left without a parallax solution in EDR3. A special attention is paid to 521 pairs with parallax known separately for both components. We find 16 entries that are deemed to be chance alignments of unrelated stars. At once we show examples of high-confidence binary systems with significant differences in the reported parallaxes of their components. Next we conclude that the reported *Gaia* EDR3 parallax errors are underestimated, at least by a factor of 3 for sources with large RUWE. Parallaxes are needed to estimate stellar masses. Since nearly 30% of ORB6 entries lack 5 or 6-parameter solution in EDR3, we attempt to enrich the astrometric data. Distant companions of ORB6 entries are revealed in EDR3 by analysis of stellar proper motions and *Hipparcos* parallaxes. Notably, in 28 cases intrinsic EDR3 parallaxes of the binary components appear to be less reliable than the parallax of the outer companions. *Gaia* DR2, TGAS and *Hipparcos* parallaxes are used when EDR3 data is unavailable. Synthetic mass-luminosity relation in the *G* band for main sequence stars is obtained to provide mass estimates along with dynamical masses calculated via Kepler’s Third Law.

Key words: parallaxes – visual binaries

1 INTRODUCTION

A pair of stars which appears close in the sky is known as a double star. [Herschel \(1803\)](#), using observations of Castor (α Gem) made in 1759 – 1803, concluded that continual change of the position angle could not be explained by the stellar proper motions. Instead, Castor together with a small companion move round their common centre of gravity. Nowadays we attribute this pair to the class of visual binary stars. Long observational sets with measurements of three parameters: time of observation, position angle, and separation between the components are needed to calculate the apparent and true orbit. This problem was analytically solved by [Savary \(1827\)](#). The orbital elements that can be derived include period P and semi-major axis a'' , deduced in angular units. Knowledge of parallax ϖ is required to convert a'' to linear measure, $a \sim \frac{a''}{\varpi}$. Then, Kepler’s Third Law $M_d \sim \frac{a^3}{P^2} \sim \frac{a''^3}{\varpi^3 P^2}$ allows one to calculate the total mass of the resolved binary. Due to large orbital periods and scarce parallax data, applicability of this method has been rather limited: while [Struve \(1837\)](#) catalogue contains 2714 double stars, [Aitken \(1918\)](#) lists 112 visual binaries with known orbits, with masses estimated for just 14 of them. The *Hipparcos* mission ([Perryman et al. 1997](#)) provided reliable parallaxes for hundreds of visual binaries; still, the double-lined eclipsing binaries remain the prime source of precise stellar masses ([Popper 1980](#); [Torres et al. 2010](#); [Serenelli et al. 2021](#)). *Gaia* space mission ([Gaia Collaboration et al. 2016a](#)) is expected

to make a breakthrough and has already brought nearly 0.8 million non-single stars including more than 165 thousand astrometric orbital solutions ([Halbwachs et al. 2022](#)) in its third data release ([Gaia Collaboration et al. 2022b](#)). Still, it represents a small fraction of binary population; particularly, 99% of the processed systems are in the 0.28 – 1500 day period range ([Gaia Collaboration et al. 2022a](#)). Largely, new non-single-star data do not overlap the long-existing observational results for visual binaries treated in this paper. *Gaia* DR3 essentially complements the EDR3 catalogue ([Gaia Collaboration et al. 2021](#)), and the content of the main table, including parallaxes, remains unaltered. It means that the presented results are completely relevant despite being based on *Gaia* EDR3. The information about known orbits of visual binaries is collected in the Sixth Catalog of Orbits of Visual Binary Stars, ORB6 ([Hartkopf et al. 2001](#)), maintained by the US Naval observatory along with the Washington Double Star catalogue ([Mason et al. 2001](#)) which is a principal catalogue for all visual binaries. ORB6 does not provide stellar parallaxes needed for mass calculation. [Malkov et al. \(2012\)](#) combined the available *Hipparcos* and ORB6 data to estimate masses. Recent *Gaia* data releases significantly improved our knowledge of stellar distances. Therefore, we attempt to supply ORB6 orbits with new available parallaxes in the present paper.

In the next Section, we briefly describe the ORB6 catalogue and our efforts to find *Gaia* counterparts for its objects. In Section 3, resolved double stars are investigated to reveal optical pairs among them and validate EDR3 parallaxes. In Section 4, we search for outer components of ORB6 binaries to expand available parallax data. Section 5 shortly describes data retrieved from other catalogues. In

* chulkovd@gmail.com

Section 6, two methods for estimating stellar masses are presented. The obtained results are discussed in Section 7. The conclusions in Section 8 are followed by Appendix A containing the complete tabulated data.

2 ORB6 BINARIES AND IDENTIFICATION IN GAIA EDR3

As of April 2022, ORB6 provides coordinates and orbital elements, including orbital period P and semi-major axis in the angular measure a'' , for 3460 entries. Apparent magnitudes useful for identification in outer data sets are available, however, these data generally are less consistent. Orbits are graded on a scale of 1–5 according to their quality, with grade 1 representing definitive orbits while grade 5 is reserved for the least reliable (undeterminate) solutions; additionally, 7 is assigned for systems with incomplete orbital elements and 8 is used for interferometric binaries. Astrometric binaries are marked by grade 9. Unfortunately, for the latter class, the perturbation amplitude (Benedict & Harrison 2017) is often published instead of a'' which should not be applied in Kepler’s Third Law, and its accidental use will cause spurious mass estimates. Dubious entries occasionally appear in ORB6 among other grades as well. We choose to keep all suspicious entries in the sample, they are manifested by unrealistic dynamical mass in Table A3.

ORB6 binaries are rather diverse, covering at least 3 orders of magnitude for P and a'' . Unfortunately, more than 40% of entries lack error estimates. For such systems, we estimate relative uncertainty of the orbit size and period according to the 75% quartile for its corresponding orbit grade. Several alternative solutions for one pair and multiple systems appear in the catalogue, notably 42 orbits are related to the Sgr A* cluster at the Galactic Center, WDS 17457-2900. The overall statistics describing ORB6 binaries as a function of their quality grade is summed up in Table 1. Along with orbital elements, predictions of angular separation ρ_{eph} and position angle for a given date are available; the authors thank Rachel Matson for providing the ephemerides at the *Gaia* EDR3 epoch.

Gaia early data release 3 (EDR3) includes 1.8 billion sources (Gaia Collaboration et al. 2021) with coordinates for the epoch J2016.0. The larger part is constructed from either 5- or 6-parameter astrometric solutions which provide information on stellar proper motions and parallaxes. The discretion between these solution types depends on the chromaticity correction method used in the processing algorithm (Lindgren et al. 2021a). Throughout this paper, we refer to both types as full solutions. In EDR3, all sources are assumed to move linearly with uniform velocity relative to the solar system barycentre, which is appropriate for single stars. Despite the absence of dedicated multiple-star solutions, *Gaia* EDR3 data are widely used for the study of binaries (El-Badry et al. 2021). Indeed, visual binaries are used for validation of EDR3 data (Lindgren et al. 2021b; Fabricius et al. 2021). 2-parameter solutions which lack parallax and proper motion values are published for the sources whose full solutions do not converge well. The quality of the full astrometric solution can be assessed with the goodness-of-fit parameter RUWE (renormalised unit weight error) which we denote χ . $\chi \approx 1.0$ for a well-behaved sources, and χ is not available for 2-parameter solutions. Unresolved binary stars are known to be manifested by a large RUWE value (Belokurov et al. 2020; Stassun & Torres 2021). When several sources within 0.18 arcsec are found by the processing algorithm, the best one is retained in EDR3 and marked as duplicated. Along with astrometric data, we use G -band photometry which is available for nearly every source (Riello et al. 2021).

More than 90% of ORB6 binaries have apparent magnitude

$\text{mag}_1 < 10.5$ in the V band; therefore, relatively bright ORB6 stars normally stand out among the field of the *Gaia* sources. Identification of *Gaia* EDR3 counterparts is based on the epoch J2000.0 coordinates provided in ORB6. The initial search is done in 1 arcsec radius with the help of TOPCAT service (Taylor 2005). For the yet unmatched binaries, the search radius is gradually increased. The majority of the sources are found within 0.5 arcsec from the reference position. However, for 52 objects, this distance exceeds 10 arcsec, most of these binaries possess high proper motions. Stellar magnitudes and WDS data on proper motions are used for confirmation of correct cross-matching when needed. ORB6 binaries often constitute a part of a multiple system. If more than one *Gaia* source is associated with the binary, the position angle and angular separation ρ is calculated. Cross-identification is carefully evaluated to prevent matching of the wrong component in the multiple system or a chance alignment star.

Depending on angular separation and apparent magnitudes, primary and secondary components may appear in EDR3 as separate sources; however, more often only one counterpart is found, see Fig 1. In such a case, the secondary source is either essentially merged with the primary or remains undetected due to large magnitude contrast with respect to the brighter primary. In multiple systems, the sampled pair can form an unresolved source with the third component. Notably, in at least ten cases, the ORB6 binary is the fainter companion of a multiple system meaning that it is essentially obscured by a brighter star in close vicinity. With a goal not to lose valuable parallax data, we choose to accept such identifications and mark them accordingly in Table A3. Generally, for the vast majority of ORB6 entries, EDR3 counterparts are readily identified. Aside from members of the Sgr A* cluster, only 26 ORB6 binaries cannot be matched, 17 of them have primary component $\text{mag}_1 < 2.7$ which is beyond the bright limit of *Gaia*. Additionally, we did not find counterparts for 9 pairs with $\text{mag}_1 \gtrsim 15$ or unknown primary magnitude in ORB6. Very faint ORB6 objects are typically red, brown, or white dwarfs and normally possess high proper motions due to their proximity to the Sun. Cross-matching of such objects is challenging, and there is a chance that at least some of them actually have unidentified 2-parameter solutions in EDR3.

Overall for 3279 unique ORB6 entries, at least one *Gaia* EDR3 counterpart is found, see Table 1. 753 pairs are resolved meaning that their components appear as separate sources in the EDR3 catalogue. *Gaia* parallaxes are available for both components in 521 pairs, these systems are discussed in Section 3. For 1016 entries, we have 2-parameter solutions meaning no parallax available in EDR3. The solution type heavily depends on the angular separation and period, see Fig. 1. Clearly, $0.2 < \rho < 0.5$ arcsec is the most difficult interval for *Gaia* leaving 2/3 of all solutions in this range with no parallax. RUWE values for 5- and 6-parameter solutions are high, confirming that these intermediate-separation binaries do not easily fit the one-star astrometric solution model of EDR3, see Fig. 2. Finally, we mention that 14 % of primary sources are marked as duplicated in EDR3. This fraction is higher for binaries with $0.05 < \rho_{\text{eph}} < 0.2$, reaching 23%. The fraction of duplicated sources among secondary stars is just 8%. For just two sources, we find the formal EDR3 parallax to be negative, in both cases the value is comparable to the reported error: WDS 06410+0954 has $\varpi_1 = -1.33 \pm 1.00$, and for WDS 17343-1909, $\varpi_1 = -0.02 \pm 0.05$. The former source additionally has excessive RUWE $\chi_1 = 5.1$.

Table 1. General properties of ORB6 binary stars as a function of the orbit’s quality grade, see Section 2. Line 1 indicates the total number of orbital solutions of the given grade. Occasionally, several solutions for the same pair are present; for subsequent statistics, only one entry per pair is chosen. The number of the unique pairs is shown in line 2. Pairs with successful cross-matching in *Gaia* EDR3 are summed up in line 3. Line 4 counts systems with EDR3 parallax for at least one component. Line 5 counts systems with primary and secondary components both appearing as separate sources in EDR3. Line 6 shows the number of systems with parallaxes available for both components. Line 7 shows the median orbital period according to ORB6. Line 8 is the 75% quartile of the relative period error, this value is used when errors are not provided for a given binary. Lines 9–10 show the median semimajor axis provided in ORB6 and its 75%-quartile relative error. Lines 11–13 list the median apparent G EDR3 magnitude, parallax, and relative parallax error of the primary components.

ü	Grade	1	2	3	4	5	7	8	9	Σ
1	Orbits	90	384	717	997	669	41	19	543	3460
2	Unique pairs	90	382	713	973	628	40	18	506	3350
3	Identified pairs	88	370	706	956	612	39	18	490	3279
4	ϖ_1 or ϖ_2	40	188	390	662	506	35	17	425	2263
5	Resolved pairs	10	34	91	295	321	–	–	2	753
6	ϖ_1 and ϖ_2	4	16	50	200	250	–	–	1	521
7	Average P , years	11.0	26.5	67.6	217	450	18.0	0.05	2.49	80
8	3/4 quartile error, %	0.1	0.9	5.0	40	49	26	< 0.1	8.9	15
9	Average a , arcsec	0.17	0.19	0.24	0.50	1.18	0.12	0.005	0.01	0.29
10	3/4 quartile error, %	0.9	2.1	5.6	25	52	4.6	3.4	25	19
11	Average primary G magnitude	5.5	7.0	7.9	8.0	8.3	8.9	5.2	6.7	7.7
12	Average parallax ϖ_1 , mas	21.7	19.4	12.1	12.1	14.0	13.5	27.5	16.3	14.4
13	Average error σ_1/ϖ_1 , %	1.6	1.6	1.9	1.1	0.5	0.2	0.4	2.0	1.3

3 RESOLVED DOUBLE STARS

The identification of resolved binaries is secure, as separation and positional angle are compared to the values predicted by ORB6 ephemerides. In a few cases, when ORB6 predictions seem erroneous, WDS data are used as well. The minimum ρ value for a *Gaia*-resolved pair is 0.20 arcsec; however, in this case, solutions for both components are 2-parameter ones. Just for 6 resolved binaries with $0.23 < \rho < 0.35$ arcsec, parallax is available for one component, while the secondary solution is a 2-parameter one. WDS 00429+2047 has minimal $\rho = 0.37$ arcsec among resolved binaries with two available parallaxes. Notably, all resolved pairs with $\rho < 0.5$ arcsec have excessive RUWE $\chi > 2.5$.

3.1 Optical pairs

ORB6 binaries are expected to be gravitationally bound. Indeed, the very presence in the ORB6 catalogue is considered *a priori* knowledge that the pair is a physical binary, and strong counter-evidence is needed to refute the claim. However, often the estimated orbital periods exceed thousands of years, which is significantly longer than the observational history. Therefore, a small number of false entries are anticipated among the ORB6 objects. If an alleged system appears in EDR3 as a resolved system with parallax and proper motion available separately for both components, we may distinguish chance-alignment pairs from genuine physical binaries.

The direct comparison of the components’ reported parallaxes ϖ_1 and ϖ_2 is possible and discussed in the next paragraph, but it appears that a more effective way to segregate optical pairs is to compare proper motions of the components. Proper motion in right ascension μ_α ¹ and declination μ_δ is provided for *Gaia* sources with available full solution. The relative proper motion of components $\Delta\mu = \sqrt{(\mu_{\alpha 1} - \mu_{\alpha 2})^2 + (\mu_{\delta 1} - \mu_{\delta 2})^2}$ can be converted to tangential speed (measured in km/s; ϖ – mas; $\Delta\mu$ – mas yr^{−1}) as:

$$v \approx \frac{4.74 \cdot \Delta\mu}{\varpi} \quad (1)$$

¹ $\mu_\alpha = \mu_{\alpha'} \cdot \cos(\delta)$, $\mu_{\alpha'}$ published in EDR3 is already corrected for $\cos(\delta)$.

The relative speed of the components should not exceed the escape velocity $v < \sqrt{2G_0M/r}$, where $r = \rho/\varpi$ is the projected distance between the components. The minimum mass required to keep the system bound is therefore calculated in SI units as:

$$M_e = \frac{\rho v^2}{2\varpi G_0} \quad (2)$$

G_0 is the gravitational constant. As we aim to find the lowest possible mass, ϖ is chosen as a maximum among components’ parallaxes ϖ_1 and ϖ_2 . The M_e distribution (Fig. 3) identifies a small number of outliers with high required masses, which must be chance alignment systems. For 16 pairs $M_e > 100M_\odot$, while for the rest of the sample, $M_e < 21M_\odot$. We neglected uncertainties of coordinates and proper motion reported in *Gaia*. Right ascension and declination errors are within 1.2 mas being too small to alter ρ . μ_α and μ_δ uncertainties are more significant as the relative error reaches 5% for a few binaries. Although real errors may be larger than reported, we do not expect them to change the outcome of optical pairs evaluation.

The comparison of parallaxes ϖ_1 and ϖ_2 further suggests that these 16 pairs are optical. As we show in Section 3.2, for a genuine ORB6 binary, the expected orbit size is negligible in comparison to the naive distance suggested from parallaxes $|1/\varpi_1 - 1/\varpi_2|$. If the measured parallax is distributed according to normal (Gauss) law with expectation ϖ_1 , ϖ_2 and standard deviation σ_1 , σ_2 for the primary and secondary component, respectively, the difference of parallaxes is expected to follow Gauss distribution as well. The particular case of equal parallaxes $\varpi_1 = \varpi_2$ has statistical significance:

$$\frac{\Delta\varpi}{\sigma} = \frac{|\varpi_1 - \varpi_2|}{\sqrt{\sigma_1^2 + \sigma_2^2}} \quad (3)$$

We use $\Delta\varpi/\sigma$ as a measure of parallax agreement for the components of ORB6 double stars. As we show in the next section, a formally large parallax disagreement does not necessarily mean the system is physically unbound. However, all 16 optical pairs candidates show $\Delta\varpi/\sigma > 8$, see Table 2. All suspicious pairs have the lowest-quality orbits (grade 5), with the exception of WDS 19054+3803 whose orbit is graded 4; therefore to find that these are chance align-

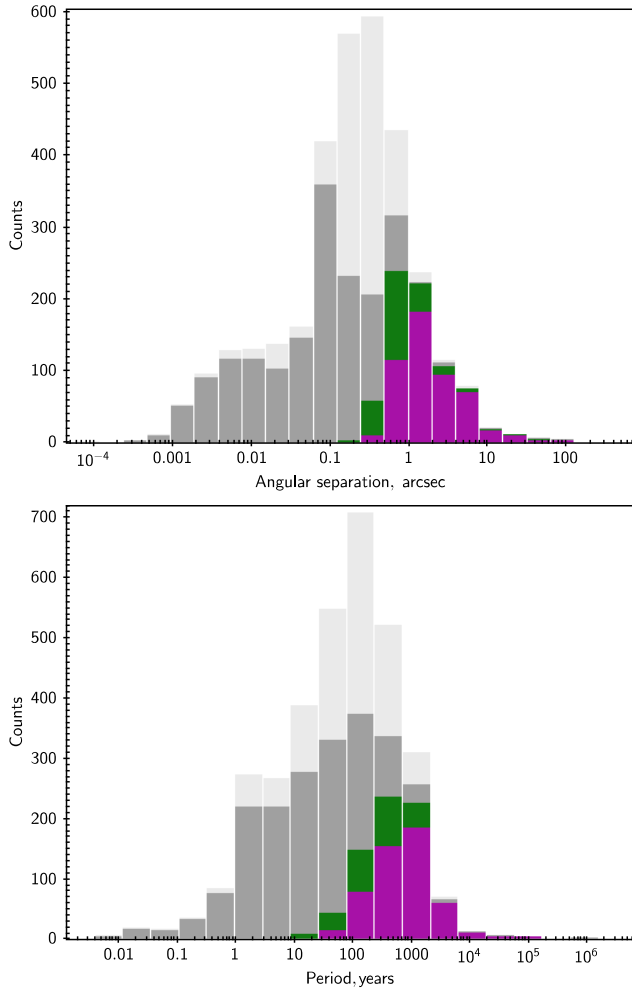


Figure 1. Distribution of ORB6 binary stars and their solution type in EDR3 as a function of ephemeris angular separation and estimated orbital period. Light gray: pairs with available solution in *Gaia* EDR3. Dark gray: systems with known EDR3 parallax. Green: resolved pairs. Purple: systems with parallaxes available for both components.

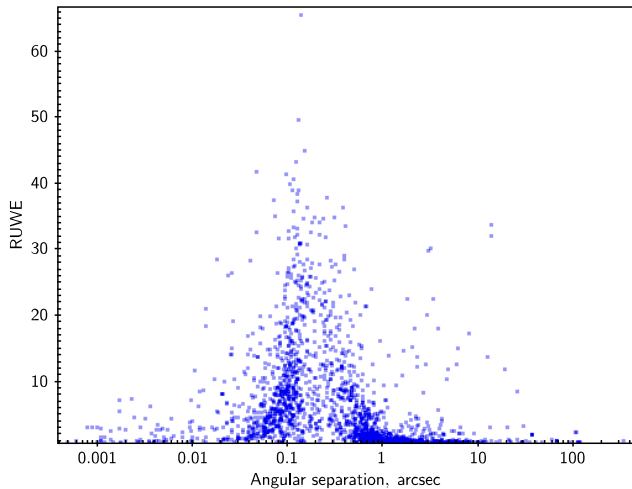


Figure 2. Primary star RUWE as a function of predicted ephemeris separation for ORB6 binaries, orbits with grade 9 are excluded.

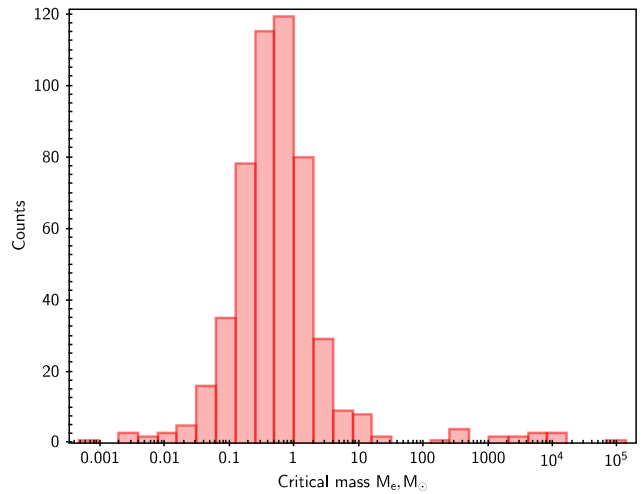


Figure 3. Minimal mass required to keep the system gravitationally bound, see Eq. 2. The subset of 521 double stars with full solutions available for both components is shown. The 16 outlier systems with $M_e > 100M_\odot$ are revealed to be likely optical pairs.

ment pairs should not come as a surprise. The minimal ρ among optical pairs is 2 arcsec in case of WDS 17248+3044.

Finally, one can argue that the critical mass M_e should not exceed the dynamical mass M_d calculated via Kepler’s Third Law, see Section 6.1 and Eq 6. Aside from the 16 likely optical pairs examined above, this condition is strongly violated by only 3 other systems: WDS 00524-6930, WDS 17419+7209, WDS 19464+3344, which have $\frac{M_e}{M_d} \sim 3 - 6$. These binaries are characterized by large $\rho > 20$ arcsec, implying that a relatively minor inaccuracy of the proper motion causes a large deviation of M_e . However, their components’ parallaxes show good agreement, $\Delta\varpi/\sigma < 1$, therefore, we do not have sufficient evidence to flag them as optical pairs.

3.2 Binaries with large parallax discrepancy

After the removal of probable optical pairs, 505 unique binaries with *Gaia* parallaxes available for both components remain in the sample. For 206 (41%) systems, ϖ_1 and ϖ_2 agree to within one standard error; for 401 (79%) pairs, the parallaxes are within 3σ , see Table 4. While the overall agreement of the parallaxes seems reasonable, these values are significantly worse than the 68.3 % and 99.7 % respectively expected from Gaussian statistics. The high number of outliers with excessive parallax disagreement is particularly remarkable. Large differences in the reported parallaxes alone do not mean that the double star is optical. 17 entries listed in Table 3 show adequate critical masses M_e and therefore are considered to be genuine binaries despite $\Delta\varpi/\sigma > 8$ which is larger than for some optical pair candidates. Below we consider some of them in greater detail, as these examples are rather instructive.

The comparison of parallaxes assumes the orbits are face-on. But in fact, the orbit of a visual binary star does not generally lie in the plane of the sky, and consequently, the distances to the components may differ slightly. This distance difference will be best measured for systems in the solar vicinity, therefore we consider WDS 05025-2115, which is a nearby binary with small reported parallax error, $\sigma_i/\varpi_i < 0.1\%$ for both components. Naive line-of-sight distance estimate between the components is $|1/\varpi_1 - 1/\varpi_2| \approx 0.05 \text{ pc} \approx 10^4 \text{ AU}$. This is by far greater than the semi-major axis estimate for this

Table 2. List of 16 ORB6 double stars that are now suspected to be optical pairs. $g_{1,2}$ are the apparent G magnitudes, ρ is the angular separation. M_e refers to minimum mass required to keep the system bound, see Eq. 2 and Fig. 3. For each entry, $M_e > 100M_\odot$ and $\Delta\varpi/\sigma > 8$ (Eq. 3). We note that WDS 19127+2435 shows an exceptionally high RUWE for both components $\chi_1 = 23$ and $\chi_2 = 30$, which strongly suggests that both sources are unresolved binaries. Additionally, there is a spurious 2-parameter source within 0.36 arcsec from the secondary star with a nearly identical magnitude, thereby, we recommend to be cautious about this system.

Designation	Magnitude		Grade	RUWE		ρ arcsec	Gaia EDR3 parallax, mas		Significance $\Delta\varpi/\sigma$	M_e M_\odot
	WDS	g_1		g_2	χ_1		χ_2	$\varpi_1 \pm \sigma_1$		
00152 + 2722	11.4	12.1	5	1.0	1.0	6.2	1.979 ± 0.025	3.522 ± 0.017	50.8	3494
03342 + 4837	7.4	11.2	5	1.0	2.0	5.6	5.936 ± 0.035	1.633 ± 0.050	70.6	491
04599 + 0031	10.7	11.2	5	1.0	1.1	6.0	1.042 ± 0.016	5.715 ± 0.021	174.1	525
05013 + 5015	9.3	9.4	5	0.9	1.0	4.2	4.367 ± 0.013	4.658 ± 0.014	15.2	310
07106 + 1543	11.6	12.0	5	1.0	0.9	10.6	12.162 ± 0.015	2.751 ± 0.014	457	522
08062 + 0201	10.8	11.1	5	1.0	1.3	2.3	3.911 ± 0.024	2.114 ± 0.028	49.5	1148
11128 + 0453	10.1	10.8	5	1.3	1.4	4.1	3.722 ± 0.023	6.346 ± 0.030	69.3	102
17121 + 2114	7.1	8.8	5	0.9	1.1	8.6	5.256 ± 0.015	2.304 ± 0.015	142	476
17248 + 3044	10.6	11.0	5	1.7	1.5	2.0	2.398 ± 0.020	2.163 ± 0.021	8.1	360
19054 + 3803	9.4	9.6	4	0.9	1.0	7.1	1.733 ± 0.010	1.611 ± 0.011	8.4	12593
19127 + 2435	8.2	11.7	5	22.7	29.9	3.6	13.059 ± 0.395	1.634 ± 0.492	18.1	113
20210 + 1028	12.2	12.4	5	1.0	0.9	6.8	0.911 ± 0.011	2.113 ± 0.011	75.2	81652
21506 + 2216	8.0	10.8	5	1.0	1.3	2.9	2.200 ± 0.023	3.544 ± 0.027	38.3	443
21559 + 3141	11.7	11.9	5	1.4	1.7	4.2	2.034 ± 0.019	2.471 ± 0.019	16.6	4143
22280 + 5742	8.8	12.7	5	1.0	1.1	45.9	0.658 ± 0.026	0.368 ± 0.013	10.0	2780
23100 + 3651	7.0	7.6	5	1.1	0.9	67.4	2.836 ± 0.022	1.428 ± 0.020	46.5	4258

Table 3. List of 17 ORB6 visual binary stars with large disagreement in the reported components' parallaxes $\Delta\varpi/\sigma > 8$ (Eq. 3), but which are still believed to be bound systems, see discussion in Section 3.2. The values of orbit quality grade and period are taken from the ORB6 catalogue.

Designation	Magnitude		Grade	RUWE		Period yr	ρ arcsec	Gaia EDR3 parallax, mas		Significance $\Delta\varpi/\sigma$	M_e M_\odot
	WDS	g_1		g_2	χ_1			χ_2	$\varpi_1 \pm \sigma_1$		
00014 + 3937	8.9	9.4	3	1.1	1.8	217	1.33	19.34 ± 0.02	20.03 ± 0.04	16.4	0.15
00076 - 0433	9.0	10.0	5	9.6	1.6	688	1.03	17.26 ± 0.32	14.15 ± 0.05	9.5	0.18
03470 + 4126	7.9	8.5	4	1.1	2.2	2276	6.88	41.90 ± 0.02	41.50 ± 0.04	8.3	0.48
05025 - 2115	7.8	9.6	3	1.8	1.8	43.6	0.89	119.57 ± 0.04	118.82 ± 0.08	8.3	0.03
06082 + 3759	7.1	9.6	5	0.9	4.0	9679	1.83	4.54 ± 0.03	2.61 ± 0.24	8.2	2.62
08582 + 1945	9.2	9.4	4	3.5	2.6	124	2.17	196.26 ± 0.20	194.14 ± 0.12	9.1	0.12
09137 + 6959	8.7	9.3	5	3.7	15.8	1469	1.15	4.96 ± 0.12	7.65 ± 0.26	9.3	4.1
09551 - 2632	8.2	8.8	5	4.3	1.5	188	0.86	18.96 ± 0.27	23.95 ± 0.05	18.0	0.37
10217 - 0946	8.1	10.2	4	3.5	1.1	1340	1.54	15.00 ± 0.08	15.71 ± 0.03	8.7	0.43
10412 - 3654	7.1	7.6	3	3.2	3.6	60.3	0.84	64.34 ± 0.05	62.62 ± 0.14	11.2	0.36
11214 - 2027	11.2	11.2	5	18.1	1.4	1028	3.81	72.86 ± 0.32	76.19 ± 0.03	10.2	0.50
11550 - 5606	4.1	5.1	5	1.9	0.9	972	3.86	31.79 ± 0.04	32.23 ± 0.02	11.1	0.25
12335 + 0901	4.9	5.6	2	14.0	6.1	15.8	1.15	223.48 ± 0.47	231.12 ± 0.51	11.0	0.01
15348 + 1032	9.6	9.6	4	3.7	1.2	1150	4.04	10.81 ± 0.50	18.97 ± 0.11	15.8	0.40
16256 - 2327	7.3	9.3	5	3.4	2.0	4193	3.00	7.26 ± 0.13	5.48 ± 0.15	8.8	17.1
20452 - 3120	12.5	12.0	5	2.3	2.3	141	2.10	100.79 ± 0.07	101.97 ± 0.08	11.2	0.40
22473 - 1609	7.3	9.3	5	8.5	1.1	824	2.65	25.49 ± 0.20	27.84 ± 0.02	11.6	0.34

binary, $a \approx \frac{a''}{\varpi} \approx 10$ AU. We conclude that the real size of the orbit is negligible in comparison to distance suggested from $\Delta\varpi$ and cannot explain the disagreement of parallaxes.

The largest parallax discrepancy in Table 3 belongs to WDS 09551-2632 with $\Delta\varpi/\sigma = 18$. However, we are confident that this system is physical due to its modest critical mass, $M_e < 1.0M_\odot$. We notice that the reported $\sigma_1 \gg \sigma_2$. Moreover, this system has an outer component at $\rho_3 = 6.2$ arcsec with $\varpi_3 = 23.95 \pm 0.02$, which perfectly matches ϖ_2 , see Section 4. Therefore, we conclude that ϖ_1 is likely to be erroneous.

Unlike optical pairs in Table 2, Table 3 contains one orbit of grade 2 and three entries with grade 3, so we are confident that these double stars are bound based on the historical observations alone. For example, the second largest $\Delta\varpi/\sigma = 16.4$ belongs to WDS 00014+3937. The values of parallaxes ϖ_1 and ϖ_2 are within 3.5%. However, the reported relative parallax errors are as small as 0.2% leading to formally high disagreement. This system has, however,

been observed since 1881, and with an estimated period 217 years it has a reliable orbit of grade 3.

3.3 Gaia EDR3 uncertainties evaluation

The agreement in the parallaxes between the two components of a system, $\Delta\varpi/\sigma$, is strongly correlated with the parameter RUWE, see Table 4. We divide the whole dataset into four equal-size subsamples according to average RUWE of components $\chi = 0.5(\chi_1 + \chi_2)$. For $\chi \leq 1.085$ subsample, 56% of parallaxes fit within one σ error, which is rather consistent with Gaussian statistics. The discrepancy is much worse for the $\chi > 2.37$ subsample, as only 21% of binaries meet the 1σ threshold.

It is remarkable that, while the Gaia-reported parallax errors σ_i/ϖ_i for stars with high RUWE are larger (Fig. 4) than for sources with small χ_i , they are still lower than what the parallax differences between components would suggest, which means that the reported

Table 4. The agreement of components' parallaxes (Eq. 3) as a function of RUWE. We consider the set of 505 binaries with full astrometric solutions available for both components; optical pairs are excluded (Section 3.1). Systems are divided into 4 equal-size groups according to average RUWE of the components, $\chi = (\chi_1 + \chi_2)/2$. 1Q: $\chi \leq 1.085$, 2Q: $1.085 < \chi < 1.341$, 3Q: $1.341 < \chi < 2.37$, 4Q: $\chi > 2.37$. The numbers of pairs in each group with parallax agreement below 5, 3, 2, and 1σ are noted; clearly the agreement is better for stars with low RUWE, see Section 3.2.

	RUWE quartile			
	1Q	2Q	3Q	4Q
Σ stars in quartile	126	127	126	126
$\Delta\varpi/\sigma < 5$	125	125	112	105
$\Delta\varpi/\sigma < 3$	118	110	93	80
$\Delta\varpi/\sigma < 2$	104	89	67	48
$\Delta\varpi/\sigma < 1$	71	62	47	26

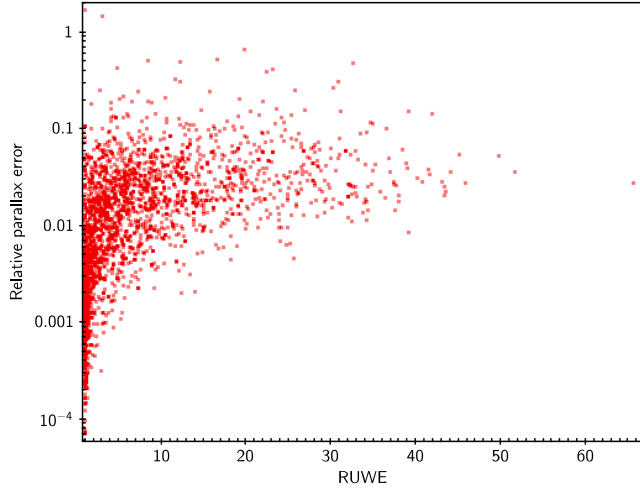


Figure 4. Reported relative parallax error σ_i/ϖ_1 as a function of RUWE for the primary components of ORB6 pairs.

σ_i values underestimate the true uncertainties, σ_i^* . We introduce a factor k , dependent on χ , to evaluate the underestimation of the reported errors. The formal *Gaia* errors for each component are multiplied by a factor $k(\chi)$, which is calculated as $\sigma_i^* = \sigma_i k$, $k > 1$, and alternate values $\Delta\varpi/\sigma^*$ are calculated from Eq. 3 for every system. Initially binaries are sorted according to the average χ of components. Next, subsamples of 100 binaries are created from consecutive entries; thus, the first sample contains the 100 binaries with the lowest RUWE, the next sample contains binaries from the 2nd to 101st, and the last² subsample contains the 100 binaries with the largest χ . The number of binaries with $(\Delta\varpi/\sigma)_i < 1$, and the average RUWE value $\bar{\chi}$, are calculated for each subsample. Then, the reported parallax errors are multiplied by the factor k which is gradually increased up to 68% of binaries within the set have $(\Delta\varpi/\sigma^*)_i < 1$. Thus, we obtain an estimate of the k factor for a value $\chi = \bar{\chi}$ from each subsample. Finally, the obtained values are averaged among 50 neighboring entries, see Fig. 5.

The underestimation factor starts at $k \sim 1.4$ for $\chi \sim 1.05$ and increases at a high rate until it reaches $k \sim 2.7$ at $\chi \sim 1.5$. Then, the relation flattens and shows moderate growth, reaching $k \sim 3.2$ for $\chi \sim 3.5$. Unfortunately, due to limited sample size, we are unable to trace $k(\chi)$ for smaller and larger RUWE. Of course, this correction

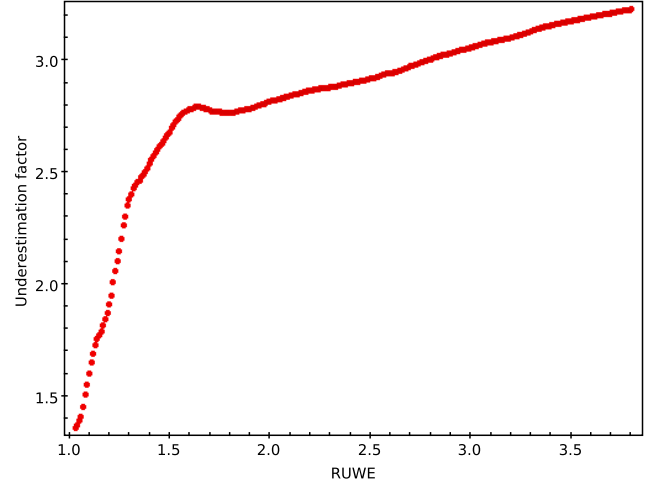


Figure 5. Parallax error underestimation factor $k(\chi)$, see Section 3.3.

should be applied with caution: the correction values k are calibrated from the one standard error deviation, thus the number of binaries with high parallax discrepancy will exceed Gauss-distribution predictions even after this correction.

4 THIRD LIGHT COMPANIONS

1016 ORB6 binaries have a 2-parameter EDR3 solution which lacks the parallax needed for a mass calculation. The absence of the desired data prompts us to use indirect methods to obtain ϖ . Many binaries are parts of multiple systems, and their parallaxes can be retrieved from the outer component which we refer to as the third light. In certain cases, the parallax of the third light ϖ_3 is more reliable than those of the binary components, ϖ_1 or ϖ_2 . In Section 3.2, we already introduced outer-companion parallax to confirm that ϖ_1 of WDS 09551-2632 is erroneous and the secondary component's parallax ϖ_2 should be used instead. However, usually we resort to ϖ_3 when both ϖ_1 and ϖ_2 are not available.

The crucial problem is to make sure that the third light is an actual companion to the system, and not a chance alignment star. Unlike with ORB6 binaries, we cannot rely on historical observations suggesting that the stars are orbiting round their common centre of mass. Kervella et al. (2022) made a comprehensive search for common proper motion candidates around *Hipparcos* stars based on their parallax and tangential velocity. The authors admit that their list is not exhaustive and misses some bound components due to rather strict conditions imposed. Our sample is not limited to *Hipparcos* objects, therefore we choose a more relaxed approach. We create a set of conditions (Eq. 4 – 5) intended to remove chance-alignment stars and apply it to every ORB6 entry. Third-light companions around binaries with known full solutions are used for validation of equations, which are restricted until no suspected unbound components make the cut. WDS provides proper motion μ_W for most of the ORB6 entries which we use as the reference and test the relation of the third light with a binary calculating the critical mass M_e with Eq. 1 and 2, adopting $\varpi = \varpi_3$ and $\Delta\mu = \sqrt{(\mu_{\alpha W} - \mu_{\alpha 3})^2 + (\mu_{\delta W} - \mu_{\delta 3})^2} = \sqrt{\Delta\mu_{\alpha}^2 + \Delta\mu_{\delta}^2}$. For binaries with available full solutions, M_e is additionally calculated according to the relative proper motion of the primary star μ_1 and the third light: $\Delta\mu = \sqrt{(\mu_{\alpha 1} - \mu_{\alpha 3})^2 + (\mu_{\delta 1} - \mu_{\delta 3})^2}$. The latter is

² 505-99=406 subsamples are created from the dataset of 505 binaries.

important as *Gaia's* μ data are expected to be more reliable than those of the WDS. For a random chance-alignment star, the critical mass is unrealistically large, therefore we constrain conditions on $\Delta\mu$ until stars with excessive M_e are gone. This procedure works fine for binaries with high μ , as their proper motions stand out among field stars. The larger precision is required for slower stars. We suspect that M_e is inadequately calculated for binaries with large RUWE reflecting the poor quality of the solution, therefore we are more tolerant to excessive values for such systems. The risk of contamination from field stars is low for close and bright components, therefore we add them without additional assumptions on proper motion. The receipt in Eq. 4 is adopted, μ is measured in mas yr^{-1} , ρ_3 is the angular distance between the third-light companion and the reference ORB6 coordinates. In the latter expression, the primary star EDR3 coordinates α_1, δ_1 are used for $\overline{\rho_3}$ calculation, g is the apparent magnitude of the third light.

$$\left\{ \begin{array}{l} |\mu| > 250, \Delta\mu_{\alpha,\delta} < 125, \rho_3 < 180'' \\ |\mu| > 200, \Delta\mu_{\alpha,\delta} < 50, \rho_3 < 180'' \\ |\mu| > 105, \Delta\mu_{\alpha,\delta} < 15, \rho_3 < 180'' \\ |\mu| > 55, \Delta\mu_{\alpha,\delta} < 5, \rho_3 < 180'' \\ |\mu| > 90, \Delta\mu_{\alpha,\delta} < 25, \rho_3 < 90'' \\ |\mu| > 30, \Delta\mu_{\alpha,\delta} < 5, \rho_3 < 30'' \\ \overline{\rho_3} < 8'', g < 10 \end{array} \right. \quad (4)$$

The comparison of parallaxes for the third light and the primary star serves as validation, see Fig. 6. Overall, 380 unique third-light components are found with Eq. 4, 130 of them are related to binaries which lack both ϖ_1 and ϖ_2 . The number of known third-light components can be increased if we introduce a reference parallax ϖ_R as *a priori* information to include those with moderate or low proper motion. Similarly to Eq. 4, conditions are carefully adjusted to reveal more genuine companions leaving aside the chance alignment stars. Although the ϖ_3 values are close to the previous ϖ_R ones, the former have better accuracy and provide an improvement for a system.

$$\left\{ \begin{array}{l} \varpi_R > 10, \frac{2\varpi_R}{3} < \varpi_3 < \frac{3\varpi_R}{2}, \Delta\mu_{\alpha,\delta} < 10, \rho_3 < 180'' \\ \varpi_R > 10, \frac{\varpi_R}{2} < \varpi_3 < 2\varpi_R, \Delta\mu_{\alpha,\delta} < 50, \rho_3 < 30'', g < 19.5 \\ \varpi_R > 5, \frac{4\varpi_R}{5} < \varpi_3 < \frac{5\varpi_R}{4}, \Delta\mu_{\alpha,\delta} < 25, \rho_3 < 100'', g < 12 \\ \varpi_R > 2, \frac{4\varpi_R}{5} < \varpi_3 < \frac{5\varpi_R}{4}, \Delta\mu_{\alpha,\delta} < 10, \rho_3 < 60'', g < 12 \end{array} \right. \quad (5)$$

The latter equation alone allows to reveal 384 or 282 third-light companions when either the *Hipparcos* parallax ϖ_{H07} (van Leeuwen 2007) or the EDR3 parallax ϖ_1 are used as the reference ϖ_R . It should be reminded that ϖ_1 is unavailable for almost 1/3 of the sample objects, therefore, the use of *Hipparcos* parallaxes is more fruitful. In 28 cases, the third-light companion is in a significant disagreement with the reported parallax of the close pair, see Fig. 7 and Table 5. If several objects are found with Eq. 4 – 5, that with the largest ϖ_3/σ_3 is chosen. We reject the high-RUWE ($\chi_3 > 1.8$) third-light source when a more reliable ($\chi_3 > 1.5\chi_1$) primary parallax exists because it can be misleading. Anyway, caution should be exercised when using ϖ_3 . It is always possible that the third light is a part of a co-moving stellar group, meaning that the line-of-sight distance can be significantly larger than the projected distance. Still we believe that these data can be helpful, especially when other sources of parallaxes are non-existent. For nine more ORB6 entries

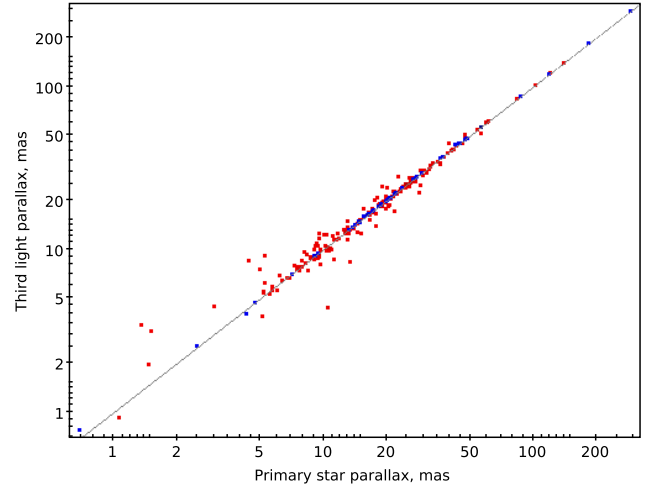


Figure 6. Parallaxes of the third-light companions processed through Eq. 4 compared to parallaxes of ORB6 primary stars. Blue dot is used when both sources have reliable low-RUWE ($\chi_{1,3} < 1.8$) solutions. Sources with larger χ (coloured red) show a larger scatter. The straight line stands for $\varpi_1 = \varpi_3$.

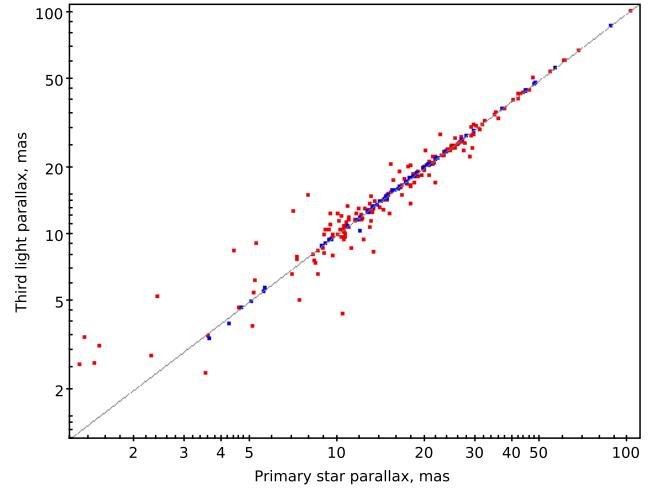


Figure 7. Parallaxes of the third-light companions processed through Eq. 5 compared to parallaxes of ORB6 primary stars. *Hipparcos* parallax (van Leeuwen 2007) serves as reference ϖ_R . Blue dot is used when both sources have reliable low-RUWE ($\chi_{1,3} < 1.8$) solutions. Sources with larger χ (coloured red) show a larger scatter. The straight line stands for $\varpi_1 = \varpi_3$.

with absent parallax data (see the next section), we identified probable third-light companions that do not strictly meet the conditions in Eq. 4. Overall, 548 unique third-light companions are found and 196 ORB6 entries with 2-parameter EDR3 solution are supplied with EDR3 parallax from the third-light component.

5 OTHER SOURCES OF PARALLAXES

889 unique ORB6 pairs are left without EDR3 parallax. Below we briefly discuss data retrieved for sample objects from other catalogues. Their proper analysis goes beyond the scope of this paper, here we restrict ourselves to several necessary remarks. We start with the predecessor *Gaia* DR2 catalogue (Gaia Collaboration et al. 2018). Around 35% of the sample sources with 2-parameter solution

Table 5. List of ORB6 binaries which have a third-light companion whose reported parallax differs significantly from that of the binary members, see discussion in Section 4 and Eq. 4–5. Systems with $\frac{|\varpi - \varpi_3|}{\sqrt{\sigma^2 + \sigma_3^2}} > 8$, $\varpi/\varpi_3 < 0.8$, or $\varpi_3/\varpi < 0.8$ are shown. ϖ is the weighted arithmetic mean of the parallax of the binary components (Eq. 7.), however, for the selected binaries ϖ_2 is not available, so ϖ_1 is used in its place. With the exception of WDS 17082-0105, all listed binaries have an unconvincing high-RUWE solution for the primary star which is refuted by the more accurate third-light parallax. *Hipparcos* parallax ϖ_{H07} (van Leeuwen 2007) is shown for the reference. We recommend to consider the use of ϖ_3 instead of ϖ_1 for the listed systems.

Designation	Parallax, mas			Significance $\frac{ \varpi - \varpi_3 }{\sqrt{\sigma^2 + \sigma_3^2}}$	RUWE		Separation ρ_3 , arcsec	Linear separation ρ_3/ϖ_3 , $10^3 AU$
	WDS	$\varpi_1 \pm \sigma_1$	$\varpi_3 \pm \sigma_3$		ϖ_{H07}	χ_1		
00046 + 4206	3.00 ± 0.35	4.43 ± 0.02	2.59 ± 0.56	4.0	10.7	1.2	5.3	1.21
00090 – 5400	4.95 ± 0.42	7.49 ± 0.07	7.79 ± 0.74	6.0	19.8	1.0	18.2	2.43
01263 – 0440	21.78 ± 0.54	17.01 ± 0.06	18.88 ± 1.98	8.8	18.3	1.1	24.6	1.45
02529 + 5300	5.09 ± 0.42	3.85 ± 0.05	3.25 ± 24.55	2.9	11.1	1.1	1.6	0.407
03184 – 2231	7.08 ± 1.47	12.63 ± 0.02	12.77 ± 1.17	3.8	10.5	1.1	29.4	2.33
04316 + 1743	28.51 ± 0.58	22.24 ± 0.02	22.76 ± 1.21	10.8	43.3	1.2	119	5.36
05133 + 0252	13.33 ± 0.31	8.30 ± 0.04	9.32 ± 0.94	16.1	4.3	1.0	6.9	0.83
05182 + 3322	9.51 ± 0.57	12.45 ± 0.04	14.04 ± 0.58	5.2	5.4	1.1	4.2	0.335
05484 + 2052	7.39 ± 0.36	5.06 ± 0.03	5.97 ± 0.73	6.5	6.2	1.3	75.4	14.9
06410 + 0954	–1.33 ± 1.00	1.40 ± 0.10	3.55 ± 0.5	2.7	5.1	1.3	3.0	2.12
06594 + 2514	2.42 ± 0.61	5.26 ± 0.03	4.48 ± 2.89	4.7	25.8	1.8	22.2	4.22
08291 – 4756	1.48 ± 0.24	1.95 ± 0.03	1.53 ± 0.34	1.9	4.2	0.9	3.5	1.78
10223 + 4130	17.80 ± 0.39	13.77 ± 0.28	14.16 ± 0.54	8.4	3.3	0.9	55.2	4.01
11151 + 3735	1.35 ± 0.41	3.44 ± 0.11	3.18 ± 1.17	4.9	12.2	1.7	0.6	0.183
11551 + 4629	10.44 ± 0.66	4.39 ± 0.02	4.72 ± 0.58	9.1	19.0	1.0	3.9	0.892
12064 – 6543	8.61 ± 0.74	6.60 ± 0.02	7.94 ± 4.49	2.7	24.1	1.0	8.8	1.33
13099 – 0532	11.18 ± 0.41	8.67 ± 0.02	10.33 ± 1.09	6.1	2.4	1.0	7.0	0.809
13123 – 5955	5.26 ± 0.82	9.10 ± 0.15	8.61 ± 0.85	4.6	14.7	3.1	1.9	0.209
15071 – 0217	12.31 ± 0.81	9.47 ± 0.13	10.50 ± 0.83	3.5	25.5	0.7	7.9	0.833
16073 – 3645	15.29 ± 0.67	20.63 ± 0.03	18.25 ± 1.05	7.9	14.3	1.5	40.4	1.96
17082 – 0105	11.91 ± 0.09	10.35 ± 0.13	11.17 ± 0.95	9.7	1.5	1.0	39.6	3.82
18232 – 6130	4.40 ± 0.89	8.43 ± 0.05	6.96 ± 1.03	4.5	5.2	1.2	3.6	0.425
18421 + 3445	1.30 ± 0.67	2.61 ± 0.03	2.19 ± 0.61	1.9	16.6	1.0	25.0	9.61
19431 – 0818	7.96 ± 0.50	15.02 ± 0.23	13.85 ± 0.63	12.7	30.0	8.8	96.6	6.43
19579 + 4216	1.52 ± 0.59	3.13 ± 0.02	3.07 ± 0.47	2.7	22.4	1.0	3.0	0.943
20169 + 5017	22.51 ± 0.41	28.00 ± 0.01	32.50 ± 0.55	13.3	24.8	1.1	106	3.78
20593 + 1534	3.54 ± 0.21	2.37 ± 0.02	2.45 ± 1.18	5.5	7.2	1.1	34.4	14.5
20598 + 4731	1.47 ± 0.37	2.63 ± 0.01	2.3 ± 0.42	3.2	2.7	0.8	20.3	7.72

in EDR3 have parallaxes available in DR2. The DR2 parallaxes are based on a shorter data-collection time, and the absence of EDR3 parallax automatically means that the DR2 parallax for a given source is potentially wrong. Still, considering that for some binaries it is the only available data source, we choose not to ignore it. Search of DR2 counterparts is based on EDR3 coordinates and is rather straightforward due to the small half-a-year difference of coordinate epochs. For more than two thousand systems, both DR2 and EDR3 parallaxes are jointly available. We use Eq. 3 as a measure of parallax disagreement with ϖ_1 and ϖ_2 standing for the reported parallaxes of primary stars in DR2 and EDR3. For 32% of primary stars, $\Delta\varpi/\sigma < 1$, and for 73%, $\Delta\varpi/\sigma < 3$. A large number of stars show enormous differences between DR2 and EDR3 parallaxes, and we expect that many DR2 parallaxes for sources with 2-parameter EDR3 solution are peculiar and therefore should be applied with caution.

The *Hipparcos* catalogue (Perryman et al. 1997), along with its revised (van Leeuwen 2007) version, provides parallaxes for most of the ORB6 binaries. Owing to dedicated solutions accounting for the non-linear motion in multiple systems, we may expect that, in certain cases, the *Hipparcos* parallaxes are more reliable than those from *Gaia* EDR3. Our sample is mostly comprised of relatively bright sources which limits *Gaia*'s superiority, and the reported *Hipparcos* relative parallax errors σ/ϖ are just half an order of magnitude larger on average. Comparing to EDR3, 59% of parallaxes meet one standard error (Eq. 3) for the original catalogue and 47% for the revised version. The most discrepant parallaxes show large RUWE in

EDR3. Two binaries (WDS 02382+4604 and 16229+3803) with no EDR3, DR2, or *Hipparcos* parallax are found in the *Tycho-Gaia* Astrometric Solution catalogue (Gaia Collaboration et al. 2016b). For the remaining 82 entries without available ϖ , we conduct a search in the SIMBAD database (Wenger et al. 2000) to obtain distance or parallax estimates for all remaining systems, the related references are provided in Table A3 of the Appendix.

6 MASS ESTIMATION METHODS

6.1 Dynamical mass

As mentioned in the introduction, Kepler's Third Law allows one to calculate the mass of a visual binary from the known orbital period and size. The derived value represents the total inside the binary's orbit, for a proper binary it is just the sum of the masses of the primary and secondary. However, the value potentially includes contribution from unseen components.

$$M_d = \frac{a^3}{P^2} = \frac{a''^3}{\varpi^3 P^2}, \quad (6)$$

where the mass is measured in M_\odot if the semi-major axis a'' and parallax ϖ are in the same angular units, and the period P is in years. When the parallaxes $\varpi_{1,2}$ of both companions are available, a

weighted arithmetic mean is used:

$$k_i = 1/\sigma_i^2; \varpi = \frac{k_1\varpi_1 + k_2\varpi_2}{k_1 + k_2}; \sigma = \frac{1}{\sqrt{k_1 + k_2}} \quad (7)$$

For the majority of ORB6 binaries, all three contributing parameters in Eq. 6 are known along with relatively large measurement errors, see Table 1. Due to error propagation, the relative uncertainties of orbit size and parallax are essentially multiplied by a factor of 3, period errors are doubled, e.g. 10% error of a'' turns into $\sim 30\%$ M_d uncertainty. Data on P and a'' are obtained from diverse methods and therefore are highly inhomogeneous. In fact, P and a'' are derived concurrently from orbital solutions, which means that their best-fit values are often correlated. Moreover, some methods use parallax for the solution of visual binary orbits (Kiyaveva et al. 2017). These factors impede uncertainty analysis and require comprehensive evaluation for each system, which is beyond our capability. We take a simplified approach to give a rough error estimate for M_d and assume all parameters to be independent. We randomly generate 10^6 values of P , a'' , and ϖ assuming Gauss distributions for uncertainties of the reported parameters. When P or a'' errors are absent for a given orbit in ORB6, the 75% quantile for the respective orbit quality grade is used. The median of the resulting sample is believed to represent the average value of M_d , while the 0.159 and 0.841 quantiles are used as confidence intervals M_d^- and M_d^+ . This approach is questionable for binaries with poorly defined orbital parameters typical of grades 4–5, and their formal error estimates and median masses are of poor credibility, therefore we also provide the value of Eq. 6 M_d^0 which completely ignores the uncertainties.

6.2 Mass – luminosity relation

The mass–luminosity relation (MLR) was originally discovered following observations of visual binary stars (Hertzsprung 1923; Russell et al. 1923) and can be used to estimate masses of main-sequence (MS) stars with known parallax and brightness. MLRs available from the literature are normally expressed in terms of bolometric or Johnson V magnitudes, and their conversion to the *Gaia* photometric system is not trivial as it depends on the stellar type. Particularly, the $G - V$ relation suggested by the *Gaia* team is invalid for red M dwarfs with $B - V > 1.3$ (Riello et al. 2021). We attempt to derive the MLR in the EDR3 photometric system using MIST (version 1.2) evolutionary tracks (Choi et al. 2016; Dotter 2016) and PARSEC (v1.2S release) isochrones (Bressan et al. 2012; Chen et al. 2014, 2015). The desired MLR should provide stellar mass as a function of absolute G magnitude. Stars of various evolutionary status and metallicity populate the MS, creating substantial dispersion in the MLR (Eker et al. 2021; Fernandes et al. 2021). Since solar metallicity $[M/H] = 0$ is typical of stars in the solar neighbourhood, which our sample belongs to, we adopt it for further calculations.

The MIST model provides absolute magnitude as a function of age for a star with a given initial mass. A dense grid of masses in $-1 < \log M/M_\odot < 2$ range with 0.01 dex step is adopted. Conveniently, the model explicitly defines zero-age and intermediate-age main-sequence (ZAMS and IAMS) evolutionary phases, therefore we acquire synthetic ZAMS and IAMS provided with stellar age, mass, and absolute V and G magnitudes. Massive stars have a relatively short lifespan; assuming smooth star formation history, their mean luminosity is expected to be represented by middle-age stars close to the IAMS³. Low-mass stars, which have a total lifespan

³ IAMS is defined as an evolutionary phase with 30% mass fraction of hydrogen in the stellar centre (Dotter 2016).

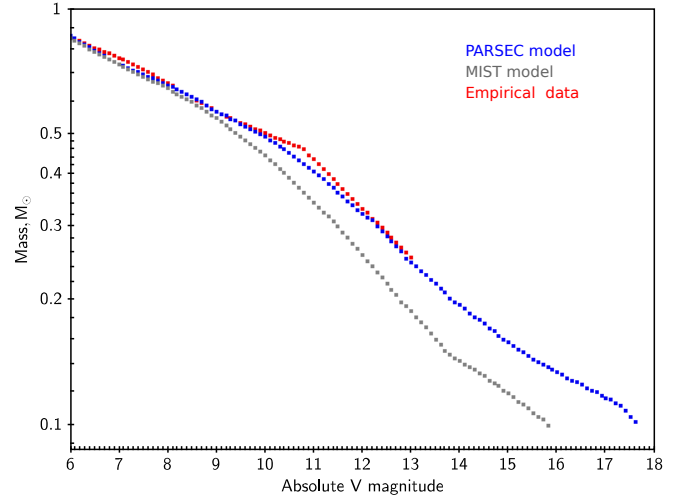


Figure 8. Comparison of synthetic ZAMS from the MIST (grey) and PARSEC (blue) models for low-mass stars, and interpolated empirical data by Eker et al. (2020) (red). The PARSEC model better fits the empirical data for the faint stars ($V > 8$ mag).

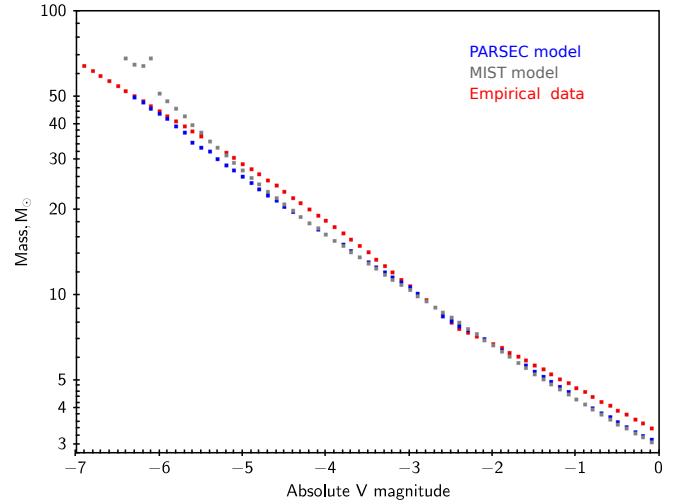


Figure 9. Comparison of synthetic IAMS from the MIST (grey) and PARSEC (blue) models for high-mass stars, and interpolated empirical data by Eker et al. (2020) (red). While both models are nearly identical, for $V < -5$ mag, the PARSEC model is clearly preferable.

comparable to or larger than the Hubble time, should be close to the ZAMS. These basic considerations are confirmed by the comparison to empirical data, see Fig. 8 and 9.

Using MIST ages and masses as input, we additionally calculate synthetic ZAMS and IAMS with the PARSEC isochrones. For this purpose, the logarithm of age is rounded to 0.01 dex precision, while absolute magnitudes are linearly interpolated as a function of mass logarithm. Thus we obtain dense synthetic ZAMS and IAMS grids for both MIST and PARSEC models which provide stellar mass as a function of absolute V and G magnitudes. We notice that synthetic ZAMS are generally consistent in both models, as predicted masses are within 2% for stars with $G < 8.5$ ($M \gtrsim 0.6M_\odot$). However, for lower masses the MIST and PARSEC models significantly diverge, see Fig. 8. In a similar way, synthetic IAMS are consistent over a wide mass range but diverge at the highest masses, see Fig. 9. For validation, we use table 6 from Eker et al. (2020), which is based on

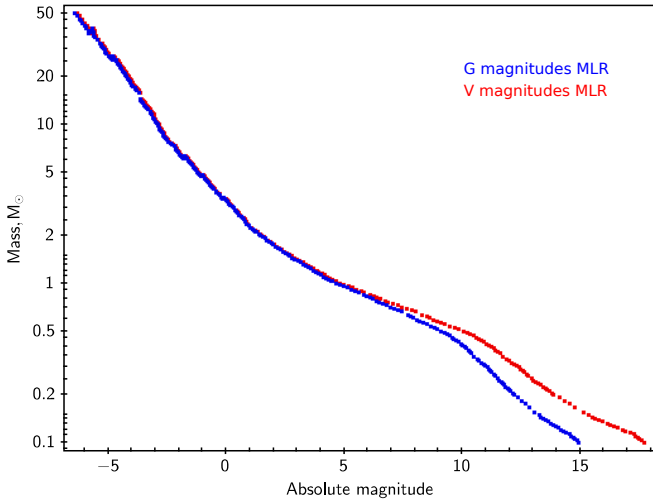


Figure 10. Mass-luminosity relations obtained in Section 6.2. The blue and red colours stand for absolute G and V magnitudes respectively. The tabulated form is available in Table A1 of the Appendix.

empirical relations and provides absolute V magnitudes for MS stars in the $0.25 M_{\odot} - 64 M_{\odot}$ range. The PARSEC model clearly shows better agreement with empirical data; therefore we adopt it for our calculations, leaving MIST as an evolutionary phase marker.

Since neither the ZAMS or IAMS alone can reproduce the empirical data for each evolutionary track, we interpolate between the ZAMS and IAMS in ten equal-age steps to obtain grids of synthetic populations with identical evolutionary phase (isophase). Next, for any given V , we select the grid line showing the best agreement of synthetic and empirical masses. As expected, the low-mass stars are better approximated by the ZAMS, while for large masses, grids with advanced evolution are preferred, and the most massive stars are best-fitted by IAMS. The transition is not completely monotonous, reflecting the limitations of synthetic tracks and empirical data. Thus, we create a composite synthetic grid closely resembling empirical MLR in the V band and apply the same isophase grids to get the G -band MLR. The resulting MLR for V and G magnitudes is shown in Fig. 10 and is available in Table A1 of the Appendix. Stars with $M < 0.1 M_{\odot}$ are not described by synthetic models, therefore, for the $0.075 M_{\odot} < M < 0.1 M_{\odot}$ range we use the updated Pecaut & Mamajek (2013) table based on (Smart et al. 2019) data. The agreement between synthetic and empirical MLR is within 0.1 mag in V -band for $M > 0.8 M_{\odot}$ and increases to 0.25 mag at the lowest masses. The intrinsic MLR uncertainty depends on stellar mass and does not exceed 38% (Eker et al. 2018, 2021) which translates into 0.35 magnitude error; however, the dispersion is approximately two times smaller for low-mass stars. Considering errors introduced by conversion to G magnitudes and intrinsic MLR dispersion, we assume a general $\sigma_{\text{MLR}} = 0.4$ mag uncertainty.

6.3 Photometric masses

The derived MLR allows us to estimate masses for our binaries. In principle, the MLR method is only applicable to MS stars with single-star evolution history; however, most ORB6 binaries meet these requirements. Despite our sample being comprised of binary stars, the large distance between components generally allows their undisturbed evolution. However, any resolved ORB6 component on its own can be a contact or semidetached binary, therefore, we should keep in mind that, in certain cases, the MLR method will yield in-

correct mass estimates. Usually the spectral classification can reveal non-MS stars. In principle, WDS provides it for most entries, however, these data are rather inhomogeneous, therefore we choose to calculate photometric masses for all entries regardless of the availability of spectral classification.

Unlike Kepler’s Third Law dynamical estimates, individual stellar masses are estimated here instead of the combined system’s mass. Depending on identification type, as discussed in Section 2, *Gaia* magnitudes can be available for one or two components. When both magnitudes are known, which is usually a case for wide systems ($\rho \gtrsim 0.5$ arcsec), masses are calculated for each component separately. If only one magnitude is available, two extreme cases are considered to define a range of possible masses: the first hypothesis is that the contribution of the secondary component is negligible and the mass of the binary is defined solely by the primary star; the second hypothesis is that the unresolved source consists of two stars of equal brightness, and the magnitude of the individual components is then assumed to be larger by $2.5 \log 2 \approx 0.75$ mag in comparison to the reported value.

Transformation from apparent to absolute magnitudes is required to enable the MLR method. First of all, saturation correction for bright stars with $g < 8$ mag is applied as prescribed in Riello et al. (2021), although its size does not exceed 0.015 mag and generally can be neglected. Then, for a star with known apparent g magnitude and parallax ϖ (measured in arcseconds), the absolute magnitude is calculated from:

$$G = g + 5 + 5 \log \varpi - A_G + \sigma_{\text{MLR}} \quad (8)$$

The following procedure is used to calculate interstellar extinction A_G . The colour excess E_{B-V} is estimated with the Stilism 3D model (Lallement et al. 2019), the input distance estimated as $1/\varpi$. Next, the V -band extinction is calculated as $A_V = R_V E_{B-V}$, $R_V = 3.1$ (Fitzpatrick 1999; Schlafly & Finkbeiner 2011). Finally, $A_G/A_V = 0.84$ conversion (Bono et al. 2019) is applied. The estimated contribution of extinction is generally low, with $A_G < 0.25$ mag for about 96% of ORB6 entries. Gauss-distributed errors $\sigma_{\text{MLR}} = 0.4$ mag are added to simulate the MLR uncertainty, with 10^6 ϖ values sampled to account for parallax error. After absolute magnitudes are calculated, the MLR (Fig. 10) is used to derive photometric masses M_p . While we stick to EDR3 photometry in Eq. 8, parallaxes are borrowed from all available sources (Section 2, 4, 5); thus, different mass estimates are possible for a given ORB6 entry depending on the ϖ value used. Arithmetic weighted means (Eq. 7) are adopted when ϖ_1 and ϖ_2 are independently known. The 0.159 and 0.841 quantiles define the confidence intervals M_p^- and M_p^+ .

7 BINARY-STAR MASSES

First, we consider 731 resolved systems with EDR3 magnitudes known for both components, enabling direct comparison of dynamical M_d and photometric M_p masses. Because Kepler’s Third Law provides the total system’s mass (Eq. 6), while MLR-derived masses (Fig. 10) are calculated for individual components, we use the sum of the primary’s and secondary’s photometric masses $M_p = M_p^1 + M_p^2$. Inconsistency between dynamical and photometric masses can be caused by various reasons including errors in ORB6 orbital elements, inaccurate parallaxes, unresolved companions, or advanced phase of stellar evolution leading to incorrect use of the MLR. In general, it may be hard to recognize which factor or their combination is

responsible for the inconsistency. Moreover, a decent agreement of M_d and M_p can occur due to lucky error aggregation.

Throughout the paper, we obtained parallaxes from various catalogues, some of which are in significant disagreement. Formal error estimates of dynamical masses are usually rather broad and several ϖ can be accepted. For a given binary we attempt to choose ϖ which provides the best agreement of M_d and M_p . We consider the ratio of dynamical and photometric masses, $r = \frac{M_d}{M_p}$ or $r = \frac{M_p}{M_d}$, $r > 1$, and choose parallax allowing the lowest r . In a favorable case when parallaxes of various origins are similar ($r_{\text{EDR3}} - r < 0.05$), we give a preference to the EDR3 parallax due to its higher accuracy. Moreover, when EDR3 and third-light parallaxes (Section 4) are comparable, that with the lower reported error is chosen. We reiterate that parallax is only one of several parameters required for mass estimation. In principle, the orbital parameters a'' and P can be adjusted instead of ϖ .

We begin with the 44 resolved binaries that have the most reliable orbits, those of quality grades 1–2, see Fig. 11. For 10 of these systems, the *Hipparcos* parallaxes are preferred over those from *Gaia* EDR3. The worst agreement of masses, $M_d = 2.92 \pm 0.04 M_\odot$ and $M_p = 1.98^{+0.15}_{-0.1} M_\odot$, is found for WDS 11182+3132 AB (ξ UMa). This star lacks *Hipparcos* and *Gaia* EDR3 parallaxes, leaving DR2 as the only available option. Overall, for 10 out of 44 binaries, M_d and M_p do not agree to within the reported uncertainties.

The rest of the ORB6 binaries have less reliable orbits and hence larger errors. As discussed in Section 6.1, the error estimates for grades 4–5 are ill-conditioned, therefore the dynamical mass M_d^0 , which ignores uncertainties, is introduced and the ratio $r_0 = \frac{M_d^0}{M_p}$, $r_0 = \frac{M_p}{M_d^0}$, $r_0 > 1$ is additionally calculated. Overall, 326 binaries with either $r < 1.2$ or $r_0 < 1.2$ are listed in Table A2 of Appendix. While 75% of orbits with grades 1–3 meet the threshold, this fraction decreases to 35% for grades 4–5, see Table 6. This fact indicates that M_d and M_p disagreements are largely caused by wrong orbital elements. Solar-type stars are the most common objects among the selected binaries, as the median primary mass is $M_p^1 = 1.05 M_\odot$, 90% of M_p^1 are in the 0.45–2.49 M_\odot range, the corresponding value for secondary stars is $M_p^2 = 0.96 M_\odot$ in the 0.35–1.89 M_\odot range. For 23 binaries with alternative orbital solutions, we choose those with the lowest r .

Most ORB6 binaries are unresolved in *Gaia* EDR3, and direct calculation of individual photometric masses is impossible for them. Instead, two extreme hypotheses are considered assuming either equal or negligible light contribution of the secondary relative to the primary component. In the latter case, obviously, $M_p = M_p^1$. If an unresolved source of the same apparent magnitude consists of two identical stars, its mass is approximately 70% larger, $\frac{M_p^=}{M_p^1} \sim 1.7$.

Such a large scatter impedes further analysis, notably the choice of the best parallax among viable options is hardly possible without additional assumptions. Any *a priori* information on the magnitude difference between the components then becomes extremely useful. For 85 pairs, more than one solution is provided in ORB6. Since duplicated entries are undesirable, we attempt to select the best among them with the use of ORB6 V magnitudes. A complete table containing mass calculations for various parallaxes is available in Table A3 of the Appendix.

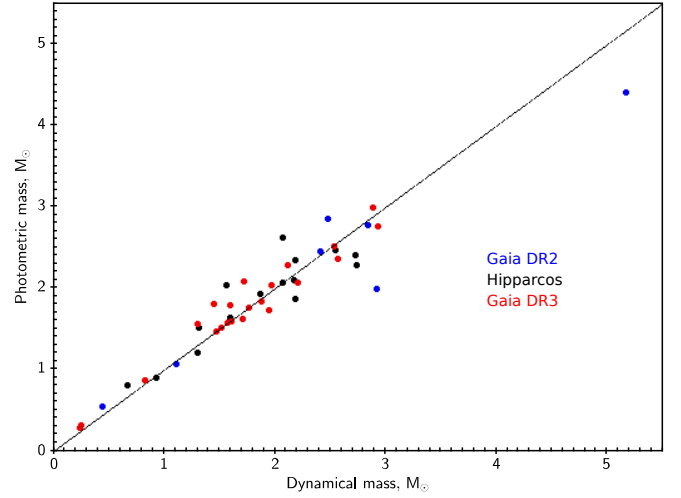


Figure 11. Comparison of dynamical and photometric masses calculated for 44 resolved binaries of grades 1 and 2. The parallax value that provides the best agreement is selected; its origin is marked in colour: black stands for original and revised *Hipparcos* parallaxes; blue – *Gaia* DR2; red – for *Gaia* EDR3.

Table 6. Agreement of the dynamical M_d and photometric M_p masses depending on the quality grade of the orbit. $r = \frac{M_d}{M_p}$ or $r = \frac{M_p}{M_d}$, $r > 1$, see Section 7 for details. Resolved systems with known magnitudes are considered.

Grade	Σ	$r < 1.2$	$r < 1.1$	$r < 1.05$
1	10	7	7	6
2	34	28	20	16
3	85	61	44	30
4	291	116	85	61
5	309	96	64	45

8 CONCLUSIONS

In the present paper, we investigate visual binary stars with known orbits from the ORB6 catalogue and use them to validate parallax error estimates of *Gaia* EDR3 and to provide stellar mass estimates for the components of the pairs. In Section 2, we search EDR3 counterparts for ORB6 entries and analyze the availability of *Gaia* astrometric solutions based on the characteristics of the binary stars (Table 1, Fig. 1–2). We show that 2/3 of the EDR3 solutions for systems with projected angular separation $0.2 < \rho < 0.5$ arcsec are 2-parameter ones and hence lack parallax ϖ . 521 resolved double stars with ϖ known for both components are discussed in Section 3. 16 optical pair candidates are revealed in Section 3.1 and Table 2. We show that large discrepancy of EDR3 components’ parallaxes reaching $\Delta\varpi/\sigma \sim 18$ does not mean that the system is unbound in Section 3.2 and give examples of such binaries in Table 3. A further analysis of reported errors is described in Section 3.3. We conclude that errors are underestimated by a factor of 3 for sources with RUWE larger than 2 (Fig. 5).

A search for outer companions of ORB6 binaries is made in Section 4 to obtain third-light parallaxes. They are found to be useful for binaries with 2-parameter solutions, and in some cases they reveal that the *Gaia* parallaxes of the primary and secondary components are unreliable (Table 5). *Gaia* DR2, TGAS and *Hipparcos* data are added in Section 5 to supply every ORB6 entry with a parallax. We proceed to dynamical mass estimation in Section 6.1. In Section 6.2, we derive a synthetic mass-luminosity relation for the G band (Fig.

10 and Table A1) which is applied to obtain photometric masses in Section 6.3. Dynamical and photometric masses are calculated for all available parallaxes of different origin. For resolved binaries, we choose the ϖ value which provides the best agreement of dynamical and photometric masses. Overall, for 326 systems, the mass estimates agree to within 20% (Table A2). The agreement is better for the most reliable orbits (Table 6, Fig. 11). A complete dataset with parallaxes and mass estimates for all entries is provided in Table A3 of the Appendix.

ACKNOWLEDGEMENTS

Authors thank Pavel Kaygorodov, Dana Kovaleva, Rachel Matson, Alexey Rastorguev and Nikolai Samus for the valuable remarks and suggestions. Elaborate review from the referee allowed to improve the paper.

DATA AVAILABILITY

The full version of tables is available in the GitHub Repository at <https://github.com/chulkovd/ORB6>.

REFERENCES

- Aitken R. G., 1918, The binary stars
 Belokurov V., et al., 2020, *MNRAS*, **496**, 1922
 Benedict G. F., Harrison T. E., 2017, *AJ*, **153**, 258
 Bono G., et al., 2019, *ApJ*, **870**, 115
 Bressan A., Marigo P., Girardi L., Salasnich B., Dal Cero C., Rubele S., Nanni A., 2012, *MNRAS*, **427**, 127
 Chen Y., Girardi L., Bressan A., Marigo P., Barbieri M., Kong X., 2014, *MNRAS*, **444**, 2525
 Chen Y., Bressan A., Girardi L., Marigo P., Kong X., Lanza A., 2015, *MNRAS*, **452**, 1068
 Choi J., Dotter A., Conroy C., Cantiello M., Paxton B., Johnson B. D., 2016, *ApJ*, **823**, 102
 Dotter A., 2016, *ApJS*, **222**, 8
 Eker Z., et al., 2018, *MNRAS*, **479**, 5491
 Eker Z., et al., 2020, *MNRAS*, **496**, 3887
 Eker Z., Soyudugan F., Bilir S., Bakış V., 2021, *MNRAS*, **507**, 3583
 El-Badry K., Rix H.-W., Heintz T. M., 2021, *MNRAS*, **506**, 2269
 Fabricius C., et al., 2021, *A&A*, **649**, A5
 Fernandes J., Gafeira R., Andersen J., 2021, *A&A*, **647**, A90
 Fitzpatrick E. L., 1999, *PASP*, **111**, 63
 Gaia Collaboration et al., 2016a, *A&A*, **595**, A1
 Gaia Collaboration et al., 2016b, *A&A*, **595**, A2
 Gaia Collaboration et al., 2018, *A&A*, **616**, A1
 Gaia Collaboration et al., 2021, *A&A*, **649**, A1
 Gaia Collaboration et al., 2022a, arXiv e-prints, p. [arXiv:2206.05595](https://arxiv.org/abs/2206.05595)
 Gaia Collaboration et al., 2022b, arXiv e-prints, p. [arXiv:2208.00211](https://arxiv.org/abs/2208.00211)
 Halbwachs J.-L., et al., 2022, arXiv e-prints, p. [arXiv:2206.05726](https://arxiv.org/abs/2206.05726)
 Hartkopf W. I., Mason B. D., Worley C. E., 2001, *AJ*, **122**, 3472
 Herschel W., 1803, *Philosophical Transactions of the Royal Society of London Series I*, **93**, 339
 Hertzsprung E., 1923, *Bull. Astron. Inst. Netherlands*, **2**, 15
 Kervella P., Arenou F., Thévenin F., 2022, *A&A*, **657**, A7
 Kiyayeva O. V., Romanenko L. G., Zhuchkov R. Y., 2017, *Astronomy Letters*, **43**, 316
 Lallement R., Babusiaux C., Vergely J. L., Katz D., Arenou F., Valette B., Hottier C., Capitanio L., 2019, *A&A*, **625**, A135
 Lindgren L., et al., 2021a, *A&A*, **649**, A2
 Lindgren L., et al., 2021b, *A&A*, **649**, A4

Table A1. Mass-luminosity relation for G band derived in Section 6.2. Excerpt, full version is available as supplementary material. The plot is shown in Fig. 10. The approximation formula $\log M = 0.497 - 0.151G + 0.0106G^2 + 2.48 \cdot 10^{-4}G^3 - 8.55 \cdot 10^{-5}G^4 - 4.13 \cdot 10^{-7}G^5 + 1.93 \cdot 10^{-7}G^6$ can be used for $-6.4 < G < 14.9$. The inverse function is $G = 4.98 - 12.6 \log M + 1.84 \log^2 M + 7.22 \log^3 M - 2.31 \log^4 M - 3.49 \log^5 M + 1.59 \log^6 M$, $0.1M_{\odot} < M < 50M_{\odot}$.

Mass, M_{\odot}	G
49.383	-6.399
47.535	-6.301
45.718	-6.199
44.840	-6.183
43.144	-6.083

- Malkov O. Y., Tamazian V. S., Docobo J. A., Chulkov D. A., 2012, *A&A*, **546**, A69
 Mason B. D., Wycoff G. L., Hartkopf W. I., Douglass G. G., Worley C. E., 2001, *AJ*, **122**, 3466
 Pecaut M. J., Mamajek E. E., 2013, *ApJS*, **208**, 9
 Perryman M. A. C., et al., 1997, *A&A*, **500**, 501
 Popper D. M., 1980, *ARA&A*, **18**, 115
 Riello M., et al., 2021, *A&A*, **649**, A3
 Russell H. N., Adams W. S., Joy A. H., 1923, *PASP*, **35**, 189
 Savary F., 1827, *Mémoire sur les orbites des étoiles doubles and Sur la détermination des orbites que décrivent autour de leur centre de gravité deux étoiles très rapprochées l'une de l'autre. Bureau des longitudes*, pp 56–69
 Schlafly E. F., Finkbeiner D. P., 2011, *ApJ*, **737**, 103
 Serenelli A., et al., 2021, *A&ARv*, **29**, 4
 Smart R. L., Marocco F., Sarro L. M., Barrado D., Beamín J. C., Caballero J. A., Jones H. R. A., 2019, *MNRAS*, **485**, 4423
 Stassun K. G., Torres G., 2021, *ApJ*, **907**, L33
 Struve F. G. W., 1837, *Stellarum duplicium et multiplicium mensurae micrometricae per magnum Fraunhoferi tubum annis a 1824 ad 1837 in Specula Dorpatensi institutae...*
 Taylor M. B., 2005, in Shopbell P., Britton M., Ebert R., eds, *Astronomical Society of the Pacific Conference Series Vol. 347, Astronomical Data Analysis Software and Systems XIV*, p. 29
 Torres G., Andersen J., Giménez A., 2010, *A&ARv*, **18**, 67
 Wenger M., et al., 2000, *A&AS*, **143**, 9
 van Leeuwen F., 2007, *Hipparcos, the New Reduction of the Raw Data*. Vol. 350, [doi:10.1007/978-1-4020-6342-8](https://doi.org/10.1007/978-1-4020-6342-8),

APPENDIX A: TABULATED DATA

This paper has been typeset from a $\text{\TeX}/\text{\LaTeX}$ file prepared by the author.

Table A2. List of resolved ORB6 binaries with decent agreement of dynamical and photometric masses. Binaries with $r < 1.2$ or $r_0 < 1.2$ are selected, see Section 7 for details. 326 systems are included. Excerpt, full version is available as supplementary material. Columns 2–4: parallax (mas) providing the lowest r , $r = \frac{M_d}{M_p}$ or $r = \frac{M_p}{M_d}$, $r > 1$. Columns 5–7: dynamical mass (M_\odot); columns 8–10: total photometric mass; columns 11–13: primary photometric mass; columns 14–16: secondary photometric mass; columns 17–19: parallax providing the lowest r_0 , $r_0 = \frac{M_d}{M_p}$ or $r_0 = \frac{M_p}{M_d}$, $r_0 > 1$. Column 20 is the dynamical mass calculated with uncertainties neglected. Columns 21–22: angular separation (arcsec) and position angle ($^\circ$).

1	2	3	4	5	6	7	8	9	10	11	12	13	14	15	16
WDS	Origin of ϖ	ϖ	σ	M_d^-	M_d	M_d^+	M_p^-	M_p	M_p^+	M_p^{1-}	M_p^1	M_p^{1+}	M_p^{2-}	M_p^2	M_p^{2+}
00014 + 3937	H97	20.42	1.91	1.24	1.70	2.38	1.61	1.72	1.84	0.84	0.90	0.95	0.77	0.83	0.88
00021 – 6817	H97	63.03	1.98	0.13	1.06	5.8	1.03	1.11	1.19	0.56	0.60	0.65	0.46	0.50	0.54
00028 + 0208	DR3	23.35	0.02	0.26	2.11	11.7	1.82	1.96	2.11	1.02	1.11	1.21	0.79	0.85	0.90
00047 + 3416	H97	6.13	1.59	1.01	3.90	18.0	3.44	4.06	5.28	1.78	2.09	2.76	1.67	1.97	2.51
00048 + 3810	DR3	10.97	0.04	0.64	1.92	6.27	1.77	1.88	1.98	0.92	0.97	1.03	0.85	0.90	0.95
1	17	18	19	20	21	22									
WDS	Origin of ϖ	ϖ	σ	M_d^0	ρ	PA									
00014 + 3937	H07	20.15	0.89	1.76	1.33	167									
00021 – 6817	DR3	58.98	0.02	1.19	4.22	131									
00028 + 0208	DR3	23.35	0.02	1.95	1.57	160									
00047 + 3416	H07	5.64	1.42	4.54	0.73	142									
00048 + 3810	DR3	10.97	0.04	1.89	0.89	28									

Table A3. Master table containing parallaxes and mass estimates for all 3460 ORB6 entries. Excerpt, full version is available as supplementary material. The lines shown are varied to avoid blank rows. Note that spurious entries with unrealistic masses are not removed from the table. Columns 1–20 comprise main orbital parameters and primary component identification in *Gaia* EDR3. Column 1: WDS designation; column 2: discoverer designation according to ORB6; columns 3–7: grade, orbital period (in years), angular semimajor axis (mas), and reported uncertainties according to ORB6. We remind that, for further calculations, the 75% quartile (Table 1) for the corresponding grade is applied when error value is absent. Columns 8–12: *Gaia* EDR3 identification, G apparent magnitude, parallax with uncertainty (mas), and RUWE of the primary star.

1	2	3	4	5	6	7	8	9	10	11	12
WDS	Designation	Grade	P	σ_P	a''	$\sigma_{a''}$	EDR3 Identification	g_1	ϖ_1	σ_1	χ_1
00000 – 1930	LTT 9831	9	1.37	0.05	0.0143	0.0028	2341871673090078592	8.94	26.80	0.51	29.4
00003 – 4417	I 1477	5	384	23	1.023	0.096	4994581292009978112	6.11			
00006 – 5306	HJ 5437	5	904	363	2.80	1.04	4972326695628963584	6.42	16.53	0.02	1.1
00008 + 1659	BAG 18	5	66.6		0.531		2772904695310603520	8.54	33.26	0.04	1.6
00014 + 3937	HLD 60	3	217	17	0.879	0.018	2881804450094712192	8.95	19.34	0.02	1.1

Table A3 – continued Secondary component in EDR3, left blank when pair is unresolved. Columns 13–17: *Gaia* EDR3 identification, G apparent magnitude, parallax with uncertainty (mas), and RUWE of the secondary star; columns 18–19: angular separation (arcsec) and the position angle ($^\circ$) according to EDR3 coordinates; column 20: disagreement of components' parallaxes (Eq 3); column 21: critical mass (Eq. 2, M_\odot); columns 22–23: average EDR3 parallax (Eq. 7, mas).

1	13	14	15	16	17	18	19	20	21	22	23
WDS	EDR3 Identification	g_2	ϖ_2	σ_2	χ_2	ρ	PA	$\Delta\varpi/\sigma$	M_e	ϖ_{EDR3}	σ_{EDR3}
00000 – 1930										26.80	0.51
00003 – 4417											
00006 – 5306	4972326695627083136	9.57	16.54	0.04	1.6	1.40	337	0.18	1.48	16.53	0.02
00008 + 1659										33.26	0.04
00014 + 3937	2881804450094712320	9.43	20.03	0.04	1.8	1.33	167	16.35	0.17	19.50	0.02

Table A3 – continued Third-light component in EDR3 (see Section 4 for details). Columns 24–28: *Gaia* EDR3 identification, G apparent magnitude, parallax with uncertainty (mas), and RUWE; column 29: angular distance (arcsec) from the primary component; column 30: projected linear separation ρ_3/ϖ_3 (10^3 AU); column 31: disagreement of primary and third-light parallax, Eq 3; column 32: critical mass (Eq. 2, M_\odot).

1	24	25	26	27	28	29	30	31	32
WDS	EDR3 Identification	g_3	ϖ_3	σ_3	χ_3	ρ_3	a_3	$\Delta\varpi/\sigma$	M_e
00003 – 4417	4994581498167873152	17.68	12.78	0.11	1.0	40.4	3.16		
00024 + 1047	2765432654808342016	8.41	10.08	0.15	4.9	63.4	6.29		
00046 + 4206	384361163100177280	9.96	4.43	0.02	1.2	5.3	1.21	4.03	5.00
00047 + 3416	2875176250406193920	10.44	4.70	0.05	2.8	95.9	20.4	1.47	10.6
00057 + 4549	386653747925624576	8.30	86.82	0.03	1.2	6.0	0.069	2.03	0.23

Table A3 – *continued* Identification in *Gaia* DR2. Columns 33–38: identification, parallax with corresponding uncertainty for primary and secondary component (mas). Columns 39–40: average DR2 parallax (Eq. 7, mas). Sources without available parallax are not provided.

1	33	34	35	36	37	38	39	40
WDS	Primary identification	ϖ_1	σ_1	Secondary identification	ϖ_2	σ_2	ϖ_{DR2}	σ_{DR2}
00000 – 1930	2341871673090078592	25.12	0.32				25.12	0.32
00003 – 4417	4994581292009978112	8.14	0.66				8.14	0.66
00006 – 5306	4972326695628963584	16.35	0.04	4972326695627083136	16.63	0.25	16.36	0.04
00008 + 1659	2772904691015625984	33.16	0.11				33.16	0.11
00014 + 3937	2881804450094712192	19.27	0.07	2881804450094712320	19.68	0.12	19.37	0.06

Table A3 – *continued* Identification in TGAS. Columns 41–46: identification, parallax with corresponding uncertainty for primary and secondary component (mas). Columns 47–48: average TGAS parallax (Eq. 7, mas).

1	41	42	43	44	45	46	47	48
WDS	id ₁	ϖ_1	σ_1	id ₂	ϖ_2	σ_2	ϖ_{TGAS}	σ_{TGAS}
00494 – 2313	2348830512245670912	50.37	0.46				50.37	0.46
00507 + 6415	524013669703057536	5.90	0.96				5.90	0.96
00524 – 6930	4691995687749952384	16.53	0.25	4691995996987597568	14.89	0.35	15.98	0.20
00542 + 4318	375705975069410176	5.25	0.24				5.25	0.24
00569 – 5153	4928347428812956416	24.54	0.52				24.54	0.52

Table A3 – *continued* Identification in *Hipparcos*. Columns 49–54: identification of primary component, Johnson *V* apparent magnitude, original (Perryman et al. 1997) and revised (van Leeuwen 2007) parallax with uncertainty (mas). Columns 55–60: the corresponding values for secondary component; columns 61–64: average original and revised *Hipparcos* parallax (Eq. 7, mas).

1	49	50	51	52	53	54	55	56	57	58	59	60	61	62	63	64
WDS	Hip ₁	mag ₁	ϖ_1^{97}	σ_1^{97}	ϖ_1^{07}	σ_1^{07}	Hip ₂	mag ₂	ϖ_2^{97}	σ_2^{97}	ϖ_2^{07}	σ_2^{07}	ϖ_{H97}	σ_{H97}	ϖ_{H07}	σ_{H07}
00053 – 0542	443	4.61	25.38	1.05	25.32	0.53							25.38	1.05	25.32	0.53
00055 + 3406	461	7.86	11.04	0.91	10.30	0.75							11.04	0.91	10.3	0.75
00057 + 4549	473	8.20	85.10	2.74	88.44	1.56	428	9.95	86.98	1.41	88.88	1.42	86.59	1.25	88.68	1.05
00059 + 1805	495	8.58	25.77	2.07	26.92	1.20							25.77	2.07	26.92	1.20
00061 + 0943	510	7.80	11.07	1.00	11.52	0.93							11.07	1.00	11.52	0.93

Table A3 – *continued* Extrananeous parallaxes applicable for pairs with absent *Gaia* and *Hipparcos* data and auxiliary information. Columns 65–67: parallax, its uncertainty, and reference (usually linked to Vizier). When σ_x is not reported, $\sigma_x/\varpi_x = 0.2$ is adopted for further calculations. Columns 68–72 are Boolean markers; column 68: identical WDS designation exists, applicable both to multiple systems and multiple solutions for the same pair; column 69: duplicated orbits for the same pair; column 70: best entry choice applicable to remove duplicated orbits; column 71: optical pair candidate (Section 3.1); column 72: merged source indicator applicable when ORB6 component is obscured by a bright star in a close vicinity. Photometric mass for such systems is unreliable.

1	65	66	67	68	69	70	71	72
WDS	ϖ_x	σ_x	Reference	b_i	b_d	b_b	b_0	b_m
00114 + 5850	1.67	0.33	J/ApJ/653/657	1	1	0	0	0
00114 + 5850	1.67	0.33	J/ApJ/653/657	1	1	0	0	0
00114 + 5850	1.67	0.33	J/ApJ/653/657	1	1	1	0	0
00114 + 5850	1.67	0.33	J/ApJ/653/657	1	1	0	0	0
00152 + 2722				0	0	0	1	0
00431 + 7659	7.74	1.55	J/AJ/156/102	0	0	1	0	0
06298 – 5014	19.44	0.66	Revised <i>Hipparcos</i> parallax of AB pair	1	0	1	0	0
11182 + 3132	114.49	0.43	<i>Gaia</i> DR2 parallax for B component	1	0	1	0	0
22385 – 1519	293.6	0.9	2010A&ARv..18...67T	1	0	1	0	1
22385 – 1519	293.6	0.9	2010A&ARv..18...67T	1	0	1	0	0

Table A3 – *continued* Dynamical and photometric masses (measured in M_{\odot}) calculated with *Gaia* EDR3 parallaxes. M_0^d : dynamical mass errors neglected. M_d : median dynamical mass with confidence interval M_d^- and M_d^+ (Section 6.1). M_p^1 : median photometric mass (Section 6.3) of primary component with confidence interval M_p^{1-} and M_p^{1+} . M_p^{2-} , M_p^2 and M_p^{2+} are the corresponding values for secondary component. M_p^2 is absent for unresolved pairs. M_p^- with error estimate M_p^{--} and M_p^{+-} is the total mass of unresolved binary in assumption of equal contribution from components. Total mass M_p of unresolved binary is therefore confined between M_p^1 and M_p^2 depending on relative magnitude contrast of components. M_p^-, M_p, M_p^+ is total photometric mass of resolved binaries.

1	73	74	75	76	77	78	79	80	81	82	83	84	85	86	87	88
WDS	M_d^0	M_d^-	M_d	M_d^+	M_p^{1-}	M_p^1	M_p^{1+}	M_p^{2-}	M_p^2	M_p^{2+}	M_p^{--}	M_p^-	M_p^{+-}	M_p^-	M_p	M_p^+
00000 – 1930	0.08	0.04	0.08	0.14	0.76	0.81	0.86				1.36	1.44	1.53			
00003 – 4417																
00006 – 5306	5.97	1.34	6.17	24.0	1.41	1.54	1.69	0.81	0.86	0.92				2.22	2.41	2.61
00008 + 1659	0.92	0.12	1.00	5.48	0.75	0.80	0.86				1.35	1.43	1.51			
00014 + 3937	1.94	1.66	1.94	2.30	0.86	0.91	0.96	0.79	0.84	0.89				1.64	1.75	1.85

Table A3 – *continued* Dynamical and photometric masses calculated with third-light EDR3 parallaxes.

1	89	90	91	92	93	94	95	96	97	98	99	100	101	102	103	104
WDS	M_d^0	M_d^-	M_d	M_d^+	M_p^{1-}	M_p^1	M_p^{1+}	M_p^{2-}	M_p^2	M_p^{2+}	M_p^{--}	M_p^-	M_p^{+-}	M_p^-	M_p	M_p^+
00003 – 4417	3.48	2.53	3.48	4.68	1.72	1.90	2.10				2.90	3.17	3.48			
00024 + 1047	2.85	0.97	2.90	9.49	1.12	1.22	1.32				1.96	2.08	2.26			
00046 + 4206	10.5	8.51	10.5	13.0	3.68	4.29	4.88				5.76	6.69	7.51			
00047 + 3416	7.87	2.67	8.01	26.2	2.21	2.59	2.99	2.07	2.29	2.71				4.28	4.88	5.70
00057 + 4549	1.91	0.25	2.07	11.4	0.56	0.60	0.65	0.49	0.53	0.56				1.06	1.13	1.21

Table A3 – *continued* Dynamical and photometric masses calculated with *Gaia* DR2 parallaxes.

1	105	106	107	108	109	110	111	112	113	114	115	116	117	118	119	120
WDS	M_d^0	M_d^-	M_d	M_d^+	M_p^{1-}	M_p^1	M_p^{1+}	M_p^{2-}	M_p^2	M_p^{2+}	M_p^{--}	M_p^-	M_p^{+-}	M_p^-	M_p	M_p^+
00000 – 1930	0.10	0.05	0.10	0.17	0.78	0.83	0.88				1.39	1.47	1.57			
00003 – 4417	13.4	9.07	13.5	19.9	2.20	2.61	3.05				3.61	4.06	4.55			
00006 – 5306	6.16	1.39	6.37	24.8	1.42	1.55	1.70	0.82	0.87	0.92				2.24	2.42	2.62
00008 + 1659	0.93	0.12	1.00	5.54	0.75	0.80	0.86				1.35	1.43	1.52			
00014 + 3937	1.98	1.69	1.98	2.34	0.86	0.91	0.96	0.79	0.84	0.89				1.65	1.75	1.85

Table A3 – *continued* Dynamical and photometric masses calculated with *Gaia* TGAS parallaxes.

1	121	122	123	124	125	126	127	128	129	130	131	132	133	134	135	136
WDS	M_d^0	M_d^-	M_d	M_d^+	M_p^{1-}	M_p^1	M_p^{1+}	M_p^{2-}	M_p^2	M_p^{2+}	M_p^{--}	M_p^-	M_p^{+-}	M_p^-	M_p	M_p^+
00494 – 2313	1.00	0.73	1.01	1.34	0.84	0.89	0.94				1.48	1.58	1.70			
00507 + 6415	3.47	2.12	3.48	6.12	3.91	4.73	5.83				6.08	7.14	8.85			
00524 – 6930	3.58	1.56	3.50	12.2	1.39	1.52	1.67	1.21	1.32	1.43				2.61	2.84	3.10
00542 + 4318	2.70	0.35	2.92	16.2	1.58	1.74	1.93				2.68	2.93	3.21			
00569 – 5153	2.01	1.68	2.01	2.40	0.80	0.86	0.91				1.43	1.52	1.62			

Table A3 – *continued* Dynamical and photometric masses calculated with original *Hipparcos* (Perryman et al. 1997) parallaxes.

1	137	138	139	140	141	142	143	144	145	146	147	148	149	150	151	152
WDS	M_d^0	M_d^-	M_d	M_d^+	M_p^{1-}	M_p^1	M_p^{1+}	M_p^{2-}	M_p^2	M_p^{2+}	M_p^{--}	M_p^-	M_p^{+-}	M_p^-	M_p	M_p^+
00053 – 0542	0.15	0.06	0.15	0.29	1.84	2.06	2.29				3.08	3.38	3.75			
00055 + 3406	0.88	0.65	0.88	1.22	1.28	1.40	1.55				2.20	2.41	2.63			
00057 + 4549	1.1	0.37	0.37	1.12	0.56	0.61	0.65	0.56	0.60	0.65				1.13	1.21	1.30
00057 + 4549	1.50	0.88	1.51	2.62	0.56	0.61	0.65	0.56	0.60	0.65				1.13	1.21	1.30
00057 + 4549	1.93	0.25	2.08	11.5	0.56	0.60	0.65	0.50	0.53	0.56				1.06	1.13	1.21

Table A3 – *continued* Dynamical and photometric masses calculated with revised *Hipparcos* (van Leeuwen 2007) parallaxes.

1	153	154	155	156	157	158	159	160	161	162	163	164	165	166	167	168
WDS	M_d^0	M_d^-	M_d	M_d^+	M_p^{1-}	M_p^1	M_p^{1+}	M_p^{2-}	M_p^2	M_p^{2+}	M_p^{--}	M_p^-	M_p^{+-}	M_p^-	M_p	M_p^+
00053 – 0542	0.15	0.06	0.15	0.29	1.85	2.06	2.29				3.09	3.39	3.75			
00055 + 3406	1.09	0.81	1.09	1.46	1.33	1.45	1.60				2.27	2.48	2.71			
00057 + 4549	0.98	0.33	1.00	3.26	0.56	0.60	0.64	0.55	0.59	0.64				1.11	1.19	1.28
00057 + 4549	1.33	0.79	1.34	2.32	0.56	0.60	0.64	0.55	0.59	0.64				1.11	1.19	1.28
00057 + 4549	1.79	0.24	1.94	10.7	0.56	0.60	0.64	0.49	0.52	0.55				1.05	1.12	1.20

Table A3 – *continued* Dynamical and photometric masses calculated with extraneous parallaxes.

1	169	170	171	172	173	174	175	176	177	178	179	180	181	182	183	184
WDS	M_d^0	M_d^-	M_d	M_d^+	M_p^{1-}	M_p^1	M_p^{1+}	M_p^{2-}	M_p^2	M_p^{2+}	M_p^{--}	M_p^-	M_p^{+-}	M_p^-	M_p	M_p^+
00114 + 5850	2.77	0.84	2.97	11.9	0.72	0.79	0.87				1.30	1.41	1.55			
00431 + 7659	10.2	1.29	11.5	74.9	1.05	1.18	1.35	0.98	1.08	1.23				2.03	2.26	2.57
00520 + 3154	0.92	0.52	0.93	1.87	0.91	0.98	1.09	0.93	1.01	1.13				1.83	1.99	2.22
06298 – 5014	2.05	1.83	2.06	2.31	0.87	0.93	0.98				1.55	1.66	1.76			
22385 – 1519	0.33	0.32	0.33	0.33	0.14	0.15	0.17				0.23	0.25	0.28			